

The added value of combining solar irradiance data and forecasts: a probabilistic benchmarking exercise

Philippe Lauret^{a,*}, Rodrigo Alonso-Suárez^b, Rodrigo Amaro e Silva^c, John Boland^d,
Mathieu David^a, Wiebke Herzberg^e, Josselin Le Gall La Salle^a, Elke Lorenz^e, Lennard
Visser^f, Wilfried van Sark^f, Tobias Zech^e

^a*University of La Réunion - PIMENT laboratory, 15, avenue René Cassin, 97715 Saint-Denis*

^b*Laboratorio de Energía Solar (LES), Departamento de Física, CENUR Litoral Norte, Udelar, Uruguay*

^c*O.I.E. Centre Observation, Impacts, Energy, MINES Paris, PSL Research University, 06904 Sophia
Antipolis, France*

^d*Industrial AI, Centre for Industrial and Applied Mathematics, UniSA STEM, University of South
Australia, Mawson Lakes Boulevard, Mawson Lakes, SA 5095, Australia*

^e*Fraunhofer Institute for Solar Energy Systems ISE, Heidenhofstr. 2, 79110 Freiburg, Germany*

^f*Copernicus Institute of Sustainable Development, Utrecht University, Princetonlaan 8a, 3584 CB, Utrecht,
The Netherlands*

Abstract

Despite the growing awareness in academia and industry of the importance of solar probabilistic forecasting for further enhancing the integration of variable photovoltaic power generation into electrical power grids, there is still no benchmark study comparing a wide range of solar probabilistic methods across various local climates. Having identified this research gap, experts involved in the activities of IEA PVPS T16¹ agreed to establish a benchmarking exercise to evaluate the quality of intra-hour and intra-day probabilistic irradiance forecasts

The tested forecasting methodologies are based on different input data including ground measurements, satellite-based forecasts and Numerical Weather Predictions (NWP), and different statistical methods are employed to generate probabilistic forecasts from these. The exercise highlights different forecast quality depending on the method used, and more importantly, on the input data fed into the models.

In particular, the benchmarking procedure reveals that the association of a point forecast that blends ground, satellite and NWP data with a statistical technique generates high-quality probabilistic forecasts. Therefore, in a subsequent step, an additional investigation was conducted to assess the added value of such a blended point forecast on forecast quality. Three new statistical methods were implemented using the blended point forecast as input.

Overall, skill scores (which quantify the relative improvement of the tested methods over a reference forecast) of methods that use the blended point forecast ranges from 42% to 46% for the intra-hour scenario and 27% to 32% for the intra-day scenario. Conversely, methods

¹International Energy Agency - Photovoltaic Power Systems - Solar Resource for High Penetration and Large Scale Applications.

that do not use the blended point forecast exhibit skill scores ranging from 33% to 43% for intra-hour forecasts and 8% to 16% for intra-day forecasts.

These results suggest that using a) blended point forecasts that optimally combine different sources of input data and b) a post-processing with a statistical method to produce the quantile forecasts is an effective and consistent way to generate high-quality intra-hour or intra-day probabilistic forecasts.

Keywords: probabilistic solar forecasting, benchmarking exercise, blended point forecast, CRPS, IEA PVPS T16

1. Introduction

Accurate forecasts of solar energy generation play a crucial role in effectively integrating solar power into existing grids and reducing associated expenses (Notton et al., 2018). This is because power output from photovoltaic plants (PV) is greatly influenced by weather conditions, making it highly variable. Consequently, having precise information about future solar power production is essential to minimize the need for costly balancing services and power reserves. Hence, enhancing solar forecasting models to increase the value of solar power generation becomes critically important. This work will focus in Global Horizontal Irradiance (GHI) forecasting since it is deemed one of the main drivers for solar power forecasting (Lorenz et al., 2021).

Today, users are faced with a myriad of forecasting methods. They can vary in the nature of the approach, the kind of inputs fed into the models, the outputs they produce or even in the forecasting horizon under consideration. Review publications aim to identify and structure all these elements, often comparing the performance values reported across the literature (Antonanzas et al., 2016; Sobri et al., 2018; Blaga et al., 2019; Yang et al., 2022). However, benchmark studies aim to do so using a methodology that ensures a fair comparison, i.e. the same locations and training and test periods. This has been done for many different aspects of solar forecasting: the post-processing of numerical weather prediction models (NWP) (Verbois et al., 2022), baseline approaches (Alonso-Suárez et al., 2022), autoregressive statistical learning approaches (Pedro and Coimbra, 2012; Lauret et al., 2015), cloud motion vector techniques (Aicardi et al., 2022), deep learning approaches using sky images as inputs (Paletta et al., 2021), among others. In other words, these benchmark studies ensure a comprehensive understanding and comparable indicators of the benefits

*corresponding author

Email addresses: philippe.lauret@univ-reunion.fr (Philippe Lauret), r.alonso.suarez@gmail.com (Rodrigo Alonso-Suárez), rodrigo.amaro_e_silva@minesparis.psl.eu (Rodrigo Amaro e Silva), John.Boland@unisa.edu.au (John Boland), mathieu.david@univ-reunion.fr (Mathieu David), wiebke.herzberg@ise.fraunhofer.de (Wiebke Herzberg), josselin.le-gal-la-salle@univ-reunion.fr (Josselin Le Gall La Salle), elke.lorenz@ise.fraunhofer.de (Elke Lorenz), l.r.visser@uu.nl (Lennard Visser), w.g.j.h.m.vansark@uu.nl (Wilfried van Sark), tobias.zech@ise.fraunhofer.de (Tobias Zech)

24 associated with a particular approach. For instance, in the frame of IEA SHC Task 46
25 (IEA-SHC-T46, 2024), Lorenz et al. (2009) designed a standardized procedure to evaluate
26 the accuracy of day-ahead deterministic irradiance forecasts.

27 However, all these previous studies focus on deterministic forecasting and dismiss the
28 inherent uncertainty of a forecast. Indeed, when it comes to decision-making for grid op-
29 erators, utilities, aggregators, balancing responsible parties and others, having not only a
30 point forecast but also an associated uncertainty or prediction interval becomes immensely
31 valuable. In other words, reliable probabilistic predictions can significantly enhance the
32 integration of variable energy sources within the energy network, leading to improved ef-
33 ficiency (Morales et al., 2014). Unlike the mature field of wind power forecasting, where
34 probabilistic forecasting is well-established (Morales et al., 2014; Iversen et al., 2015; Jung
35 and Broadwater, 2014; Pinson et al., 2007), probabilistic solar forecasting is still relatively
36 nascent (Hong et al., 2016; van der Meer et al., 2018; Hong et al., 2020). Consequently,
37 there are considerably less benchmark studies focusing on solar probabilistic forecasts.

38 A literature review restricted to intra-hour/intra-day solar probabilistic forecasts reveals
39 that a few studies have started to address this gap. Among others, one can cite the fol-
40 lowing works. Grantham et al. (2016) used a non parametric bootstrapping method for
41 generating prediction intervals of GHI at a forecast horizon of 1h. The bootstrap tech-
42 nique requires a point forecast which is, in their work, delivered by a linear auto-regressive
43 (AR) model. With only past ground data, David et al. (2016) used a combination of point
44 forecast ARMA model and a parametric GARCH model to generate intra-hour (up to 1h
45 ahead with a time step of 10 mins) and intra-day (up to 6h ahead with a time step of 1h)
46 GHI probabilistic forecasts. Lauret et al. (2017) evaluated the quality of three probabilis-
47 tic models for intra-day solar forecasting. A linear quantile regression technique is used to
48 build three models for generating 1 to 6h ahead probabilistic forecasts. Inputs of the models
49 are either only ground data or ground data with day-ahead forecasts provided by the Eu-
50 ropean Center for Medium-Range Weather Forecast (ECMWF). The results demonstrated
51 that the Numerical Weather Prediction (NWP) exogenous inputs improve the quality of the
52 intra-day probabilistic forecasts. Using only past ground GHI measurements, David et al.
53 (2018) set up a combination of 3 points forecasting methods and 7 probabilistic methods
54 to issue intra-day GHI forecasts. None of the model combinations clearly outperformed the
55 others. However, regardless of the point forecasting method used, linear models in quantile
56 regression, weighted quantile regression and gradient boosting decision trees appear to pro-
57 duce probabilistic forecasts with higher quality than the other proposed methods. In their
58 work, Alonso-Suárez et al. (2020) developed three models aimed at generating intra-day
59 probabilistic GHI forecasts, spanning lead times from 10 minutes to 3 hours with a gran-
60 ularity of 10 minutes. The initial model solely relies on historical ground measurements.
61 The second model enhances the first one by integrating a variability metric derived from
62 these historical ground measurements. The third model incorporates satellite albedo as an
63 additional input. A linear quantile regression is employed to create directly (i.e. without
64 using a point forecast) a range of quantiles summarizing the predictive distributions of the
65 global solar irradiance. The findings demonstrate that the inclusion of satellite data further
66 enhances the quality of the probabilistic forecasts. Mazorra-Aguilar et al. (2021) assessed

67 the performance of two approaches for solar probabilistic forecasting to generate intra-day
68 solar forecasts covering time horizons from 1 hour to 6 hours. The first approach involves a
69 two-step process. Initially, point forecasts are generated for each forecast horizon, followed
70 by the utilization of quantile regression techniques to estimate the prediction intervals. The
71 second methodology directly predicts the quantiles of the predictive distribution using past
72 ground data as input. Yang et al. (2020) benchmarked 5 forecasting intrahour/intraday
73 solar probabilistic methods (including notably an Analog Ensemble method and a linear
74 quantile regression technique) on a standardized dataset set up by (Pedro et al., 2019). All
75 the proposed methods generate directly the quantile forecasts without resorting to a point
76 deterministic forecast. The findings clearly highlight the significance of exogenous inputs
77 in probabilistic solar forecasting, as all methods demonstrate enhanced results upon the
78 integration of exogenous features computed from sky, satellite images and NWP outputs
79 provided by the NAM the North American Mesoscale (NAM) forecast system.

80 Finally, it must be noted that specific methods based on Cloud-Motion Vector (CMV)
81 approach or combination of sky and satellite images have been recently proposed in the
82 literature. For instance, Carrière et al. (2021) designed a CMV-based probabilistic method
83 which is an extension of the deterministic CMV approach by adding Gaussian noise to
84 the norm and direction of the cloud motion vector estimates. Paletta et al. (2023) used
85 an hybrid deep learning method combining sky images, satellite observations and/or past
86 ground irradiance to generate intra-hour solar forecasts.

87 Following the previous literature review, the following comments can be made. To evalu-
88 ate the quantile forecasts two methodologies can be distinguished. The first one leverages on
89 a point deterministic forecast to produce with a specific statistical technique the prediction
90 intervals. The second one generates directly (i.e. without resorting to a point forecast) the
91 quantile forecasts. Regarding the first methodology, no work tries to evaluate the impact of
92 a high quality point forecast on the generation of probabilistic forecasts.

93 Moreover, to the best of our knowledge, no benchmarking exercise has been conducted
94 to compare classical probabilistic techniques like quantile regression or Analog Ensemble
95 with a CMV-based probabilistic approach on multiple sites experiencing different climate
96 conditions.

97 Therefore, as part of IEA PVPS T16 (IEA-PVPS-T16, 2024), experts engaged in Activity
98 3.3 on solar probabilistic forecasts found it essential to complement these previous studies
99 regarding intra-hour and intra-day solar probabilistic forecasts. In other words, it appears
100 important to experts of the IEA PVPS T16 to propose to the solar forecasters community
101 a comprehensive benchmarking exercise related to intra-day and intra-hour solar irradiance
102 forecasts.

103 To this end, five participants set-up a benchmarking exercise based on a shared ground
104 measurement, satellite and NWP data. Eight European sites with diverse climatic condi-
105 tions were chosen for this purpose. The proposed benchmarking procedure is implemented
106 to compare 15-min irradiance probabilistic forecasts up to 6 hours issued by each participant
107 with their own forecasting methods. In particular, to fill the gaps highlighted by the litera-
108 ture review, it appeared first important to the IEA PVPS experts to jointly evaluate a CMV
109 probabilistic system with traditional quantile forecasting methods. Second, an assessment

110 of the impact of a high quality point forecast on the quality of the generated probabilistic
111 predictions is also conducted in this work.

112 To evaluate the quality of the probabilistic predictions, different diagnostic tools and
113 scoring rules can be employed (Lauret et al., 2019). For user convenience, the verification
114 scheme should be kept simple. For that, we propose using the reliability diagram as a
115 visual diagnostic tool and the Continuous Ranked Probability Score (CRPS), as the numer-
116 ical score. It is commonly adopted by the community in the verification process of solar
117 irradiance probabilistic forecasts.

118 Further, in this work, unlike most of the previous studies, and in order to better highlight
119 the skill of a forecasting method, we propose the numerical decomposition of the CRPS into
120 the reliability and resolution components as in (Lauret et al., 2019).

121 The rest of the paper is organized as follows. Firstly, this paper introduces the bench-
122 marking exercise. Section 3 details the data used in the exercise while Section 4 gives an
123 overview of the diverse forecasting methodologies. The verification framework is presented
124 in Section 5. Section 6 gives the main results of the benchmark and Section 7 discusses
125 the impact of combining a blended point forecast with statistical techniques to generate
126 probabilistic solar forecasts. Finally, Section 8 concludes this paper.

127 **2. The benchmarking exercise**

128 In the frame of the IEA PVPS Task 16 (IEA-PVPS-T16, 2024), five participants agreed
129 to set up a benchmarking exercise related to intra-day and intra-hour solar irradiance prob-
130 abilistic forecasting. Table 1 lists the participants of this benchmark, the code that will be
131 used to identify them throughout the following sections and plots, as well as the forecasting
132 methods used. For this exercise, each participant submitted their forecasts under the form
133 of quantile forecasts (i.e. the quantiles of the predictive distribution).

134 Together, the participants designed the framework that would guide this benchmark,
135 namely the type of input data that could be fed into the forecasting models, the forecast
136 horizons to be considered, and the selection of the probability levels of the quantile forecasts.
137 Table 2 gives details regarding these decisions. Thus, each participant was responsible for
138 generating 15-min irradiance probabilistic forecasts up to 2 hours ahead (for intra-hour)
139 and up to 6h (for intra-day) for 8 selected European sites (described in Section 3). The
140 verification of the forecasts was conducted blindly by one of the authors of this paper. The
141 MAE, equivalent to the CRPS of a deterministic forecast, of the median of the predictive
142 distribution was included in order to evaluate the improvement of CRPS brought by the
143 probabilistic approaches over their deterministic counterparts.

Participant	Code/Method	Forecasting methodology	Input data
Mines Paris (OIE)	OIE	CMV-based probabilistic approach	Satellite data
University of La Réunion (PIMENT)	PIMENT	Parametric method ARMA-GARCH	Ground data
Fraunhofer (ISE)	ISE	Blended point forecast + Analog Ensemble	Ground + satellite + NWP data
Utrecht University (UU)	UU	Non-linear Quantile Regression Forest	Ground data
Laboratorio de Energía Solar (Udelar)	LES	Linear quantile regression	Ground + satellite data

Table 1: List of participants. The code associated to each participant also identifies the forecasting methodology used by the participant

Type of Input Data	<ul style="list-style-type: none"> - Ground GHI measurements - Satellite estimates - NWP forecasts - Solar geometry variables (e.g. Solar Zenith Angle (SZA), etc)
Forecast horizon	<ul style="list-style-type: none"> - Intra-hour: 8 horizons (15 to 120 min, in 15-min steps) - Intra-day: 16 horizons (135 to 360 min, in 15-min steps)
Forecasts specification	15 GHI quantile forecasts with probability levels of [0, 0.025, 0.05, 0.1, 0.2, 0.3, 0.4, 0.5, 0.6, 0.7, 0.8, 0.9, 0.95, 0.975, 1]
Verification metrics	<ul style="list-style-type: none"> - Reliability diagram - CRPS - CRPS skill score with the CSD-CLIM model as baseline - see (Le Gal La Salle et al., 2021). - MAE of the median of the predictive distribution

Table 2: Parameters of the benchmarking exercise. Details regarding the verification metrics are provided in section 5

144 3. Data for the benchmarking exercise

145 3.1. Ground measurements

146 It is crucial to use identical data for evaluation when comparing various prediction meth-
147 ods. The selected dataset comprises 15-min measured GHI values from eight locations of
148 Europe. We restricted the evaluation to European sites since the methods of two of the
149 participants used satellite data only covering most of the European domain. The evalua-
150 tion period spans from January 2017 to December 2018. The year 2017 was chosen for the
151 training set of the different methods described below, while 2018 was used for testing these
152 methods.

153 The original reference database comprises high temporal resolution GHI data (1 minute)
 154 that were collected for a benchmarking exercise of modelled solar radiation data (Forstinger
 155 et al., 2021). This benchmark exclusively incorporates quality-assured data, meticulously
 156 checked using an extensive range of best practices and newly established quality-control
 157 procedures (Forstinger et al., 2021). These procedures encompass automated and manual
 158 data quality tests along with descriptive quality flagging, conducted by a team of experts of
 159 the IEA PVPS T16 subtask 1 (IEA-PVPS-T16, 2024).

160 The 15-min dataset results from a downsampling of these original 1-min. More precisely,
 161 the 1-min raw GHI were averaged at 15 minutes resolution. Also, in case of missing raw data,
 162 a linear interpolation is done if the gap is below 1h otherwise the whole day is discarded.
 163 Finally, data for which solar elevation $\leq 10^\circ$ have been filtered out and are consequently not
 164 taken into account in the evaluation process.

165 Table 3 gives all the details related to each site. Note that, except for the TAB site
 166 provided by CIEMAT/DLR (CIEMAT, 2024), all sites are part of the BSRN (BSRN, 2024).

Site	Code	Latitude ($^\circ$ N)	Longitude ($^\circ$ E)	Altitude (m)	Köppen C.	Source	Mean GHI (W/m^2)
Cabauw	CAB	51.9711	4.9267	0	Cfb	BSRN	315.0
Carpentras	CAR	44.083	5.059	100	Csa	BSRN	411.1
Cener	CEN	42.816	-1.601	471	Cfb	BSRN	381.6
Milan	MIL	45.4761	9.2545	150	Cfa	RSE	394.1
Palaiseau	PAL	48.713	2.208	156	Cfb	BSRN	347.7
Payerne	PAY	46.815	6.944	491	Cfb	BSRN	368.9
Plataforma Solar	TAB	37.0909	-2.3581	500	Bsk	CIEMAT/DLR	499.5
Toravere	TOR	58.254	26.462	70	Dfb	BSRN	318.1

Table 3: Locations and key figures of ground measurements used for the benchmark. Column "Köppen C." lists the Köppen-Geiger climate classification of each site while column "Mean GHI" gives the average GHI of the test dataset.

167 3.2. Satellite data

168 In this study, two data sets of GHI estimates based on satellite data are considered. Both
 169 are based on images obtained by the SEVIRI instrument onboard the Meteosat Second Gen-
 170 eration (MSG) satellite using the MSG 15-minute visible channel with a spatial resolution
 171 of approximately 1×2 km at Europe.

172 The first data set used for the OIE and LES forecasts is derived from the satellite images
 173 using the Heliosat-4 model (Qu et al., 2017a). The GHI estimates in the second data set
 174 used for the ISE forecasts are based on a modified version of the Heliosat method (Hammer
 175 et al., 2003).

176 Generally, for forecasting purposes, a sequence of satellite images is used to infer cloud
 177 motion vectors (CMV), i.e. vectors that describe cloud advection, which can be extrapolated
 178 into the future to make a prediction. For a better understanding of the assumptions and
 179 limitations of the use of CMV, the reader is directed to (Lorenz et al., 2021).

180 3.3. NWP forecasts

181 NWP forecasts are used as input to generate blended point forecasts by ISE. Thereto,
182 ISE includes the atmospheric model high resolution 10-day forecast (HRES) product of the
183 ECMWF IFS forecast with a spatial resolution of 0.125° and a time resolution of 1 h. The
184 forecast of shortwave solar radiation downwards (ssrd) is used at base-times 0:00 UTC and
185 12:00 UTC. It is spatially smoothed over 9x9 grid points, and upsampled from the original
186 1 h time resolution to 15 min via clear sky index (see Equation 1) interpolation.

187 4. Description of the probabilistic methods

188 Let us recall that all probabilistic methods depicted in this work generate quantile fore-
189 casts with the probability levels given in Table 2. However, each participant utilizes their
190 own method to produce this set of quantiles (listed and briefly described above in Table 1).

191 Three classes of approaches are employed in this benchmark. The first class extends
192 to the probabilistic domain a framework traditionally used to produce deterministic CMV-
193 based forecasts, mainly by adding Gaussian noise to its inputs (similarly to a Monte Carlo
194 approach). That is the case of Mines Paris OIE. The second class corresponds to a two-step
195 approach where a deterministic forecast is generated and then used as input by a statistical
196 technique to generate the quantile forecasts. This is the case of participants PIMENT and
197 ISE. Conversely, the third class produces directly (in one step) the quantile forecasts from
198 a set of input variables. This is the case of participants UU and LES.

199 Finally, in the field of solar forecasting, it is a standard procedure to detrend the Global
200 Horizontal Irradiance (GHI) time series due to its non-stationary nature, characterized by
201 daily cycles and annual seasonalities (Lauret et al., 2022). This detrending process involves
202 utilizing the output of a clear sky model. Specifically, a new deseasonalized series, known as
203 the clear sky index k_c time series, is derived by employing the following data transformation

$$k_c = \frac{I}{I_c}, \quad (1)$$

204 where I is the measured global horizontal irradiance and I_c is the output of a clear sky
205 model. All the proposed forecasting models described below make use of the clear sky index
206 k_c time series. However, it should be noted that the choice of the clear sky model may vary
207 depending on the participant.

208 4.1. Description of Mines Paris OIE model

209 This approach, proposed originally in Carrière et al. (2021), combines physical and sta-
210 tistical elements and leverages a standard satellite-based solar forecasting framework which
211 is traditionally used for deterministic forecasting. Figure 1 gives an overview of the principle
212 of the method.

213 First, a 25x25 grid with 0.04° resolution centered in the location of interest is defined.
214 For each grid cell, satellite-derived time series for GHI and its clear-sky expectation (I_c) are
215 obtained from the Copernicus Atmospheric Monitoring Services (CAMS) Radiation product
216 (Qu et al., 2017b) using the pvlib Python interface (Jensen et al., 2023). Note that while

217 the native resolution of this product depends on the distance to nadir, the CAMS Radiation
218 product adjusts to any requested coordinates by means of interpolation. Based on this data,
219 the corresponding clear-sky index k_c grid was calculated according Equation 1 and its spatial
220 resolution was further increased by a factor of 3 through a 2D linear interpolation. Then,
221 the CMV of each downscaled k_c cell is inferred using an Optical Flow technique following
222 the work of Chow et al. (2015) and using an efficient method proposed by (Liu, 2009).

223 Deterministic CMV-based forecasts are calculated, for example, by extrapolating the k_c
224 grid in space (according to the CMVs and the forecast horizon) and selecting the advected
225 k_c value which is closest to the location of interest. In this approach, an Eulerian spa-
226 tial extrapolation is considered, where the clouds are assumed to move in a straight-line
227 trajectory.

228 Here, the probabilistic aspect is enabled by three elements: i) a Gaussian noise distri-
229 bution relative to the CMV estimates, namely to the norm and direction of a vector; ii)
230 a Gaussian noise distribution relative to the k_c estimates; and iii) a monitoring perimeter.
231 The first two aim to describe the uncertainty associated with the estimation of the satellite-
232 derived variables, whereas the third defines a distance threshold below which an extrapolated
233 grid cell is considered a plausible forecast candidate. This allows the generation of a set of
234 plausible advection scenarios. The third corresponds to a distance threshold below which an
235 extrapolated k_c pixel is considered a plausible forecast candidate. Thus, the combination of
236 the viable candidates from all the generated scenarios constitutes an ensemble of k_c forecasts
237 from which an empirical CDF is built.

238 Finally, the k_c CDF is converted back to GHI by multiplying it with the I_c obtained from
239 CAMS Radiation (see Equation 1), which considers the McClear clear-sky model, which
240 accounts for water vapor and aerosol effects (Lefèvre et al., 2013). To mitigate potential
241 calibration issues, the forecasts are post-processed by first considering the baseline model
242 CSD-CLIM (Le Gal La Salle et al., 2021) for defining the bounding quantiles (Q0 and Q100)
243 and then implementing a quantile mapping approach for calibration, adjusting the effective
244 probability rate of each quantile to its theoretical rate according to the training data.

245 More details on this implementation can be found in Carrière et al. (2021), including the
246 parameters assumed for the considered sources of Gaussian noise. Concerning the model
247 implementation, a few remarks:

- 248 • It is only tested for the locations covered by the CAMS Radiation service (i.e., covered
249 by the Meteosat Second Generation geostationary satellite);
- 250 • It is only tested for the horizon range between 15 minutes and 2 hours;
- 251 • In two situations, the baseline approach proposed by (Le Gal La Salle et al., 2021)
252 is considered instead of the CMV-based one: i) when for a given day, forecast time,
253 and horizon, there is yet no available satellite image; ii) when this approach leads to
254 less than 50 k_c candidates, which possibly compromises the representativeness of the
255 produced ensemble.

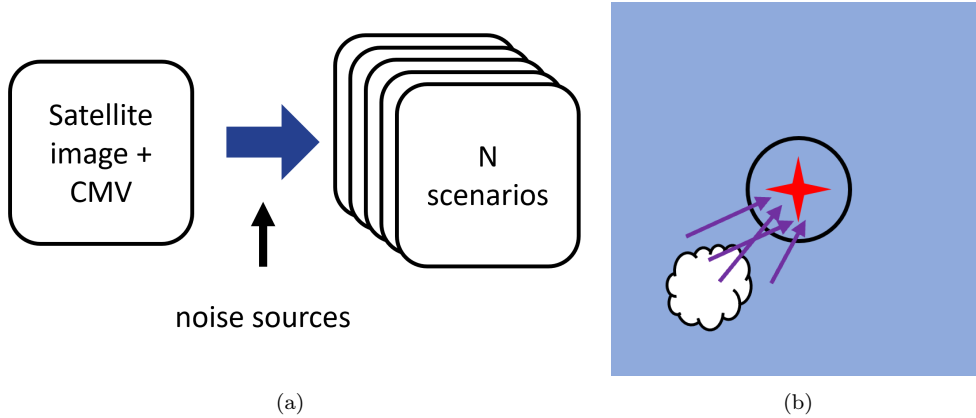


Figure 1: Mechanisms leveraging the probabilistic CMV approach: (a) the generation of advection scenarios by inputting noise to the base CMV; (b) the consideration of all advected grid cells that fall inside a monitoring perimeter.

256 4.2. Description of PIMENT model

257 The PIMENT model is based on a parametric approach commonly used in the financial
 258 domain. It combines a AutoRegressive Moving Average model (ARMA) and Generalized
 259 AutoRegressive Conditional Heteroskedasticity (GARCH), which successively generate a
 260 point forecast and then its associated uncertainty. This combination in the field of solar
 261 energy has been first introduced by David et al. (2016). The model is applied to the clear
 262 sky index k_c time series with the McClear model (Lefèvre et al., 2013) selected as the clear-
 263 sky model .

264 The AutoRegressive Moving Average model (ARMA) stands as a prevalent and widely-
 265 applied method in time series prediction. Its extensive utilization in forecasting renewable
 266 energy has underscored its competitive edge, owed largely to its parsimonious nature. No-
 267 tably, its application spectrum encompasses the forecasting of solar irradiance among other
 268 domains (Bacher et al., 2009; David et al., 2018). A general formulation of an ARMA(p,q)
 269 model with p autoregressive (AR) terms and q moving average (MA) terms is given by
 270 (Tsay, 2010). Its application to the h -ahead forecast of a variable y is given by the following
 271 equation

$$\hat{y}_{t+h} = \alpha_0 + \sum_{i=1}^p \alpha_i \times y_{t-i+1} + \sum_{j=1}^q \beta_j \times \epsilon_{t-j+1}, \quad (2)$$

272 with $h = 1, 2, \dots$ the forecast horizon and $\alpha_0, \alpha_1, \dots, \alpha_p, \beta_1, \dots, \beta_q$ the coefficients to be
 273 estimated. The error term ϵ is the difference between the previous forecasts and observations
 274 as defined in the following equation:

$$\epsilon_t = \hat{y}_t - y_t. \quad (3)$$

275 The ARCH (AutoRegressive Conditional Heteroskedasticity) models, introduced by En-
 276 gle (Engle, 1982), is used to model the variance of time series in the financial domain. These
 277 models are particularly efficient to predict changes in variance over the time, for instance

278 the error of point forecast generated with an ARMA model (Bollerslev, 1986). PIMENT
 279 applied the Generalized AutoRegressive Conditional Heteroskedasticity (GARCH) model
 280 proposed by Bollerslev (1986), which gives a more parsimonious formulation than the sim-
 281 ple ARCH model. In GARCH models, the conditional variance is a linear function of lagged
 282 squared error terms and also lagged conditional variance terms (Taylor, 2004). The general
 283 formulation of a GARCH(r,s) model, with r error terms, s conditional variance terms and
 284 an horizon of forecast h, is given by:

$$\hat{y}_{t+h} = \hat{\sigma}_{t+h} \times \varepsilon_t, \quad (4)$$

285 with ε an uniformly distributed random variable with a null mean and a unitary variance,
 286 and $\hat{\sigma}_{t+h}$ the predicted standard deviation given by

$$\hat{\sigma}_{t+h}^2 = \gamma_0 + \sum_{i=1}^r \gamma_i \times \varepsilon_{t-i+1} + \sum_{j=1}^s \delta_j \times \sigma_{t-j+1}^2. \quad (5)$$

287 As for the ARMA models, $\gamma_0, \gamma_1, \dots, \gamma_r, \delta_1, \dots, \delta_s$ are the coefficients to be estimated.
 288 There are numerous methods to estimate these coefficients. The two most widely used are
 289 the least squares (LS) and the Maximum Likelihood Estimation (MLE) methods. Here, we
 290 propose to implement the Recursive Least Squares (RLS) method, which is a variation of
 291 the LS method. This method reduces the computational cost with the coefficient of the
 292 model being updated in real-time as new data become available. The RLS method is very
 293 efficient in an operational context where forecast have to be timely delivered.

294 To determine the lag parameters p, q of the ARMA model, PIMENT ran the model on
 295 the training year for different combinations of the lag parameters with values varying from
 296 1 to 10. The best combination is the one that minimizes the RMSE of the point forecast.
 297 For the probabilistic part, PIMENT used a GARCH(1,1), which is appropriate for the error
 298 times series of the point forecast.

299 4.3. Description of Fraunhofer ISE model

300 The approach by Fraunhofer ISE consists of two steps. In a first step, blended point
 301 forecasts are derived from different input data (Section 4.3.1). In a second step, quan-
 302 tile forecasts are generated from these blended point forecasts using the Analog Ensemble
 303 (AnEn) method (Section 4.3.2).

304 4.3.1. Blended forecasts by Fraunhofer ISE

305 Deriving blended forecasts from several distinct input forecasts using statistical or ma-
 306 chine learning methods is a common approach in deterministic forecasting (see e.g. Lorenz
 307 et al., 2021).

308 Here, GHI forecasts are generated by blending three different types of forecasts

- 309 • a persistence forecast,
- 310 • a satellite-based forecast,
- 311 • and the deterministic ECMWF IFS forecast (see Section 3.3).

312 The persistence forecast is created by deriving a clear sky index from the latest mea-
 313 surement, which is then extrapolated into the future. Fraunhofer ISE employs the clear-sky
 314 model from Dumortier (1995) and the turbidity model from Bourges (1992) to compute
 315 clear sky irradiance and the clear sky index, not only for persistence, but for all modeling
 316 steps described in this section. The satellite-based forecasts are based on CMVs derived
 317 from MSG satellite images (see section 3.2) following Kühnert et al. (2013). The CMVs
 318 are computed using a block matching algorithm. Future images are obtained by repetitive
 319 application of the cloud motion vectors. Finally, smoothing filters depending on forecast
 320 lead times are applied to the future images.

321 The three different forecast types are blended using a set of linear regression models,
 322 fitted for each forecast horizon and time of the day. This allows to adjust the regression
 323 weights to the varying performance of the different input forecasts in dependence of the
 324 forecast horizon (see Figure 2). The resulting blended forecast can be written as

$$I_{\text{blend}}^{h,\tau} = c_{\text{pers}}^{h,\tau} \cdot I_{\text{pers}}^{h,\tau} + c_{\text{cmv}}^{h,\tau} \cdot I_{\text{cmv}}^{h,\tau} + c_{\text{nwp}}^{h,\tau} \cdot I_{\text{nwp}}^{h,\tau}, \quad (6)$$

325 where I_X are the GHI of the blended, persistence, CMV or NWP forecast, c_X are the
 326 corresponding regression weights, and h and τ denote the index of the forecast horizon and
 327 time of the day respectively. When determining the regression weights $c_X^{h,\tau}$ for a forecast
 328 horizon h , data from $h \pm 2$ horizons were included in the fit, to enable the generation of
 329 a smooth blended output forecast from the different linear models. The regression weights
 330 are trained for the year 2017 and applied to generate the forecasts for 2018. With multiple
 331 sites of observation and forecast data, either one set of the blending parameters for all sites
 332 or separate sets for each site can be derived. It was decided for the single site training, to
 333 obtain close-to-bias-free blended forecasts for each site.

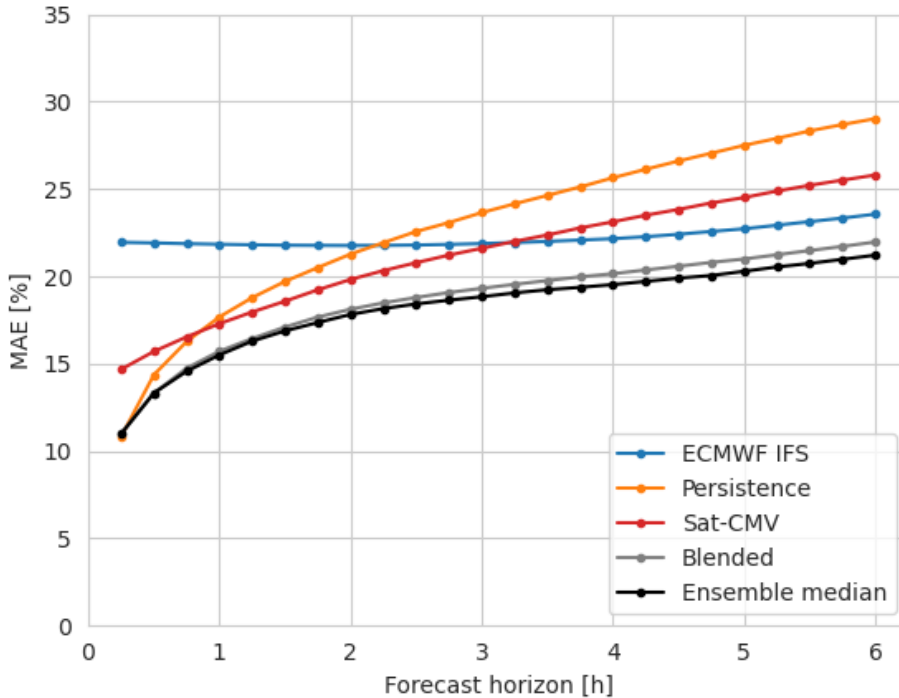


Figure 2: Relative MAE vs. forecast horizon, computed for all eight sites together for the test year of 2018. The MAE is normalized with the average GHI, which differs between 351 W/m^2 and 397 W/m^2 depending on filtering. Filtering such that all component forecasts for blending are available; the deviations of the ensemble median here compared to the benchmark (e.g. Figure 4) result from differences in the filtering.

334 When generating the blended forecasts, missing data is handled in the following way:
 335 If one of the component forecasts is missing, a simple mean of the remaining component
 336 forecasts is calculated instead of using the regression weights. For horizons or times of the
 337 day for which no regression weights could be determined, NWP data is returned. It should
 338 be noted here that persistence as well as satellite based forecasts can only be calculated after
 339 sunrise and before sunset, which impacts availability of these forecasts in the early morning
 340 hours depending also on the forecast horizon. For example, if the earliest satellite based
 341 forecast could be calculated at 7:00 am, forecasts for horizons of 4 hours ahead are available
 342 only from 11:00 am onwards.

343 The performance of the different forecasts, quantified in terms of MAE, is shown as a
 344 function of forecast horizon in Figure 2. Here the different availabilities of the forecasts
 345 discussed above have to be considered. For reasons of comparability, calculation of MAE
 346 includes only data points for which all displayed forecasts are available. The Figure shows
 347 that the persistence forecasts are best performing for short horizons up to 45 minutes,
 348 satellite-based forecasts are best performing for intermediate horizons up to about 3 hours,
 349 and the NWP performs best for even larger horizons. The blended forecasts always exhibit
 350 a lower MAE than any of the individual input forecasts. They form the basis to derive

351 probabilistic forecasts in a next step.

352 4.3.2. Analog Ensemble

353 The Analog Ensemble (AnEn) is a non-parametric ensemble prediction method (Delle Monache
354 et al., 2013; Junk et al., 2015). The method is based on the evaluation of historic observa-
355 tions and deterministic forecasts. Past forecasts are compared to the current forecast and
356 the observations corresponding to the most similar forecast situations, called analogs, then
357 form an ensemble of possible future values. The quantities, which are used to measure sim-
358 ilarity, are called predictors. Alessandrini et al. (2015) constructed an AnEn for PV power
359 prediction and used the GHI, solar elevation and azimuth, cloud cover, and ambient tem-
360 perature (T2M) from the deterministic ECMWF IFS forecast as predictors. Here, an AnEn
361 to predict the GHI instead of the PV power is created. Furthermore, just one predictor
362 quantity is used for the AnEn, namely the forecasted clear sky index.

363 To set up the Analog Ensemble, in a first step, the clear sky index values of the blended
364 forecasts and the measurements are computed. Situations with measurement-based clear sky
365 index values above 1.2 are excluded. To identify the analogs for a current forecast value with
366 a forecast horizon h_0 , similarity to past forecasts is evaluated using the Euclidean distance
367 of the forecast values of five horizons $\{h_0 - 30\text{min}, h_0 - 15\text{min}, h_0, h_0 + 15\text{min}, h_0 + 30\text{min}\}$,
368 centered around h_0 . This window helps to reduce fluctuations in the distance measure and
369 to improve meteorological similarity between situations. The measurement-based clear sky
370 indices corresponding to the 40 most similar situations are taken to form the AnEn.

371 Similar to a k-nearest-neighbor regression, the AnEn has no explicit training phase,
372 instead the analogs are selected from a search space at the time a prediction is made. The
373 analog search is performed separately for each forecast horizon and each time of the day,
374 reflecting different uncertainties in dependence of the forecast horizon (see Fig. 2) and the
375 time of the day. The search space for the analogs is composed using a rolling window of the
376 last 180 days and integrating all eight European sites together, resulting in 1440 historic data
377 points from which the 40 analogs are selected. Integrating the different sites increases the
378 search space and thus the reliability of the ensemble. It is made possible by using the clear
379 sky index as a predictor instead of GHI and close-to-bias-free forecasts for the different sites.
380 The ensemble of clear sky indices is, then, transformed back to GHI values by multiplication
381 with clear sky irradiance. The quantiles are finally obtained by a linear interpolation of the
382 ensemble members, see method 7 of (Hyndman and Fan, 1996).

383 4.4. Description of Utrecht University (UU) model

384 Quantile regression forest (QRF) is a nonlinear ensemble model that is based on the
385 random forest regression (RF) model (Koenker, 2005; Meinshausen and Ridgeway, 2006).
386 Similar to a RF model, QRF is made up of a predefined set of decision trees that exist of
387 a number of layers (t_n) and decision nodes ($2t_n$). The trees are constructed independently
388 from each other by considering bootstrap samples from the training dataset in the training
389 stage. The nodes are constructed by selecting a random subset of the predictor variables
390 and optimizing the decision node on a preset loss function, e.g the mean squared error. In
391 contrast to a RF model, the QRF model predicts a conditional distribution function (or

392 weighted distribution of observations). Hence, given a set of predictor variables, each tree in
393 the QRF model predicts the conditional quantiles of the target variable, i.e., GHI. Finally, a
394 post-processing step is added in which each quantile value is set to be equal or higher than
395 zero and equal or lower than the clear sky irradiance estimate (I_c).

396 The UU forecast model follows the approach described in Visser et al. (2023) to find the
397 optimal hyperparameter settings. Hence, the training set is split into several training and
398 validation subsets, using k -fold cross-validation with $k = 8$ (Raschka and Mirjalili, 2019).
399 Once the optimal hyperparameter settings are found, the QRF model is trained considering
400 the entire training set, i.e., one year (2017) and then applied to predict the GHI for the test
401 year (2018).

402 The QRF model considered in this study operates endogenously. This implies that the
403 model only relies on historical observations of the target variable, i.e., the GHI (I), as well as
404 variables that are available at any time, i.e., the clear sky irradiance I_c . Using I and I_c , we
405 construct two additional variables: the clear-sky index k_c (see Equation 1) and the expected
406 GHI using a clear sky-based smart persistence model, similar as discussed in Section 4.3.

407 From these four main variables, a large set of predictor variables can be generated by
408 simply considering a multitude of lagged values. In this study, UU optimizes the number
409 of historical values by means of an iterative process. Hence, starting with a base model,
410 at each iteration one lagged value is added, where after an evaluation if the addition leads
411 to a significant performance improvement is made. The final set of variables considers 18
412 predictor variables, including: the previous eleven GHI measurements ($I(t), (\dots), I(t - 10)$),
413 the clear-sky irradiance ($I_c(t + k)$), the clear-sky index ($k_c(t)$) and the persistence forecast
414 considering the three most recent irradiance measurements ($I_{pers}(t + k, t), I_{pers}(t + k, t -$
415 $1), I_{pers}(t + k, t - 2)$).

416 4.5. Description of Udelar LES model

417 The LES forecast is an adaptation of the methodology proposed by Alonso-Suárez et al.
418 (2020). This approach utilizes lagged ground measurements and geostationary satellite data
419 as inputs for a Linear Quantile Regression (LQR) model, as described by Koenker and
420 Bassett (1978). The LQR model is used to predict quantiles of the clear-sky index (k_c). These
421 quantiles are then converted to quantiles of the Global Horizontal Irradiance (GHI) using the
422 McClear clear-sky model (see Equation 1). While the mathematical formulation is relatively
423 simple, the crucial aspect lies in the predictors' selection. The forecasting model incorporates
424 the present time and the six preceding k_c values, along with four other predictors derived
425 from either the past k_c values or a satellite space cell that surrounds the specific location.
426 The first additional predictor is the local short-term variability (σ_c), which is calculated as
427 the standard deviation of the last six changes in k_c . For more in-depth information on how
428 σ_c is calculated, please refer to Alonso-Suárez et al. (2020). The remaining three predictors
429 are derived from the Heliosat-4 satellite estimates in a 25×25 px space cell provided by the
430 Copernicus Atmosphere Monitoring Service (CAMS). By employing the McClear model, the
431 clear-sky index is calculated for each pixel in the satellite cell. From this index, the average,
432 standard deviation, and cloud coverage are computed and utilized as input variables in
433 the LQR method. The cloud coverage is estimated as the fraction of pixels in the cell

434 with $k_c < 0.85$. In summary, the inputs for the LQR model are six lagged k_c values, the
435 local short-term variability, and four variables related to the current time. These current
436 time variables consist of the measured k_c , the space average and standard deviation of the
437 satellite-derived k_c , and the satellite-estimated cloud coverage within the cell. Different LQR
438 parameters are trained for each site, forecast horizon, and quantile.

439 5. Proposed evaluation framework

440 Visual diagnostic tools and quantitative scores are used to assess the quality of the
441 probabilistic forecasts (i.e. the correspondence between ground truth and the forecasts).
442 Diagnostic tools are used to visually assess the quality of probabilistic forecasts, while nu-
443 merical scores are used to quantify the skills of a forecasting system and to rank competing
444 prediction methods.

445 In this study, following the recommendation of Lauret et al. (2019), we adopt the CRPS
446 as the scoring rule to assess the overall performance of the forecasting method. Moreover,
447 to gain a deeper understanding of the forecast skill of each forecasting method, we further
448 decompose the CRPS into two components: reliability and resolution. In case of predictive
449 distributions summarized by discrete quantile forecasts, Lauret et al. (2019) proposed specific
450 formulae to compute the CRPS and its related decomposition. The interested reader is
451 referred to (Lauret et al., 2019) for more details regarding the computation of this CRPS
452 decomposition. Another useful assessment is whether a prediction system outperforms a
453 trivial baseline model. To this end, we compute the CRPS skill score with the climatological
454 model CSD-CLIM (Le Gal La Salle et al., 2021) as the reference model.

455 Finally, in this work, we use reliability diagrams to visually evaluate reliability of the
456 different forecasts.

457 5.1. Visual assessment with reliability diagrams

458 The reliability diagram serves as a graphical tool for assessing the reliability of probabilis-
459 tic forecasts. In this paper, we follow the methodology established by (Pinson et al., 2010),
460 which is tailored for predictive distributions summarized by quantile forecasts. Specifically,
461 quantile forecasts are considered reliable when their stated probabilities match the observed
462 proportions. In essence, over a sufficiently large evaluation dataset, the disparity between
463 observed and nominal probabilities should be minimized (Pinson et al., 2010).

464 One of the advantages of this representation is that it allows deviations from perfect
465 reliability, represented by the diagonal line, to be readily visualized (Pinson et al., 2010).
466 However, it's important to acknowledge that due to the finite sample of observation/forecast
467 pairs and potential serial correlation in the sequence of forecasts and observations, observed
468 proportions may not align precisely along the diagonal, even if the forecasts are perfectly
469 reliable (Pinson et al., 2010). In other words, reliability diagrams can sometimes be mis-
470 leading because even for perfectly reliable forecasts, deviations from the ideal diagonal case
471 can be observed.

472 To address the limitations arising from the finite number of observation/forecast pairs,
473 (Bröcker and Smith, 2007) introduced reliability diagrams with consistency bars. Addition-
474 ally, Pinson et al. (2010) has proposed consistency bars that consider the combined effects of

475 serial correlation and limited data. In this work, consistency bars are calculated according
 476 to (Pinson et al., 2010). When interpreting reliability diagrams with consistency bars, it
 477 becomes clear that one cannot reject the hypothesis of the quantile forecasts being perfectly
 478 reliable if the observed proportions fall within the consistency bars. In practice, incorporat-
 479 ing consistency bars into reliability diagrams can provide additional support for the user’s,
 480 possibly subjective, assessment of the reliability of the different models.

481 5.2. Continuous Rank Probability Score (CRPS) and its decomposition

482 The Continuous Ranked Probability Score (CRPS) is a numerical score that quantifies
 483 the difference between the predicted and observed cumulative distribution functions (CDF)
 484 (Hersbach, 2000). It is formulated as follows:

$$\text{CRPS} = \frac{1}{N} \sum_{i=1}^N \int_{-\infty}^{+\infty} \left[\hat{F}_{fcst}^i(x) - F_{x_{obs}}^i(x) \right]^2 dx, \quad (7)$$

485 where $\hat{F}_{fcst}(x)$ is the predictive CDF of the variable of interest x (e.g. GHI) and $F_{x_{obs}}(x)$ is a
 486 cumulative-probability step function that jumps from 0 to 1 at the point where the forecast
 487 variable x equals the observation x_0 (i.e. $F_{x_{obs}}(x) = 1_{\{x \geq x_{obs}\}}$). The squared difference
 488 between the two CDFs is averaged over the N observation/forecast pairs.

489 The CRPS score is designed to reward forecasts that concentrate their probabilities
 490 around the step function located at the observed value, promoting accuracy and precision
 491 in forecast predictions (Wilks, 2009). Put simply, the CRPS serves as a penalty for both
 492 insufficient resolution in predictive distributions and biased forecasts. It is worth noting that
 493 the CRPS is oriented negatively, meaning that smaller values indicate better performance,
 494 and it has the same unit as the forecast variable.

495 As previously mentioned and in accordance with its nature as a proper scoring rule
 496 (Gneiting and Raftery, 2007), the CRPS can be decomposed into two fundamental aspects
 497 of probabilistic forecasts: reliability and resolution. This decomposition of the CRPS yields
 498 the following equation:

$$\text{CRPS} = \text{REL} + \text{UNC} - \text{RES}. \quad (8)$$

499 The reliability REL component of the CRPS provides an assessment of forecast biases,
 500 while the resolution RES component quantifies the improvement achieved by issuing case-
 501 dependent probability forecasts. The uncertainty component UNC, on the other hand, is
 502 inherent to the observations and cannot be influenced by the forecast system; it depends
 503 solely on the variability of the observed data (Wilks, 2009).

504 Given that the CRPS is negatively oriented, the objective of a forecast system is to
 505 minimize the reliability component as much as possible, while also maximising the resolution
 506 component. By employing this decomposition of the CRPS, a detailed evaluation of the
 507 forecast performance of different forecasting methods can be obtained.

508 Besides, in the case of deterministic forecasts, the CRPS reduces to the Mean Absolute
 509 Error (MAE). This characteristic enables a direct comparison between the performance
 510 of a probabilistic model and a deterministic one, or equivalently, it allows for assessing

511 the additional value provided by a probabilistic approach (Ben Bouallègue, 2015). In this
 512 study, we calculate the Mean Absolute Error (MAE) of the forecast distribution’s median
 513 to evaluate the extent to which the probabilistic approach enhances (or fails to enhance) the
 514 overall quality of the forecasts over its deterministic counterpart.

515 *5.3. The CSD-CLIM model and the associated CRPS skill score*

516 Probabilistic scores do not allow fair comparisons between different sites or datasets. To
 517 do so, it is a good practice to consider the relative performance against reference models
 518 (Gneiting et al., 2023) through skill scores. Over the past years, several benchmark models
 519 for probabilistic forecasting were introduced in the literature (Doubleday et al., 2020; Gneit-
 520 ing et al., 2023). For this work, the CSD-CLIM model has been selected. For each site, the
 521 measurements of the training dataset are gathered according to a set of bins of clear-sky
 522 irradiance. Then, empirical CDFs are built independently for each bin. In the test period,
 523 the clear-sky model is used to select the appropriate bin and the associated forecasting CDF.
 524 Thus, the CSD-CLIM approach is climatological in the sense that it only uses historical data
 525 and a clear-sky model. More details about theory and implementation are available in (Le
 526 Gal La Salle et al., 2021). In this work, the McClear clear-sky model (Lefèvre et al., 2013)
 527 has been chosen with 30 clear-sky irradiance bins.

528 A skill score represents the degree of improvement of a forecasting model compared to
 529 the reference baseline model. The CRPS skill score (CRPSS) reads as

$$\text{CRPSS} = 1 - \frac{\text{CRPS}_{\text{model}}}{\text{CRPS}_{\text{reference}}}. \quad (9)$$

530 **6. Results**

531 *6.1. Reliability diagrams*

532 Reliability diagrams related to each scenario (intra-hour or intra-day) for each participant
 533 are given in Figure 3, with each of the plots averaged for all sites. Note that the averaging
 534 for all sites is performed by aggregating GHI observations and forecasts for each site into two
 535 distinct time series. This procedure will be also used to calculate the overall CRPS results
 536 in section 6.2.1. Consistency bars for a 90% confidence level are individually computed for
 537 each nominal proportion. Note that comments related to Figures 3f, 3g and 3h will be made
 538 in Section 7.

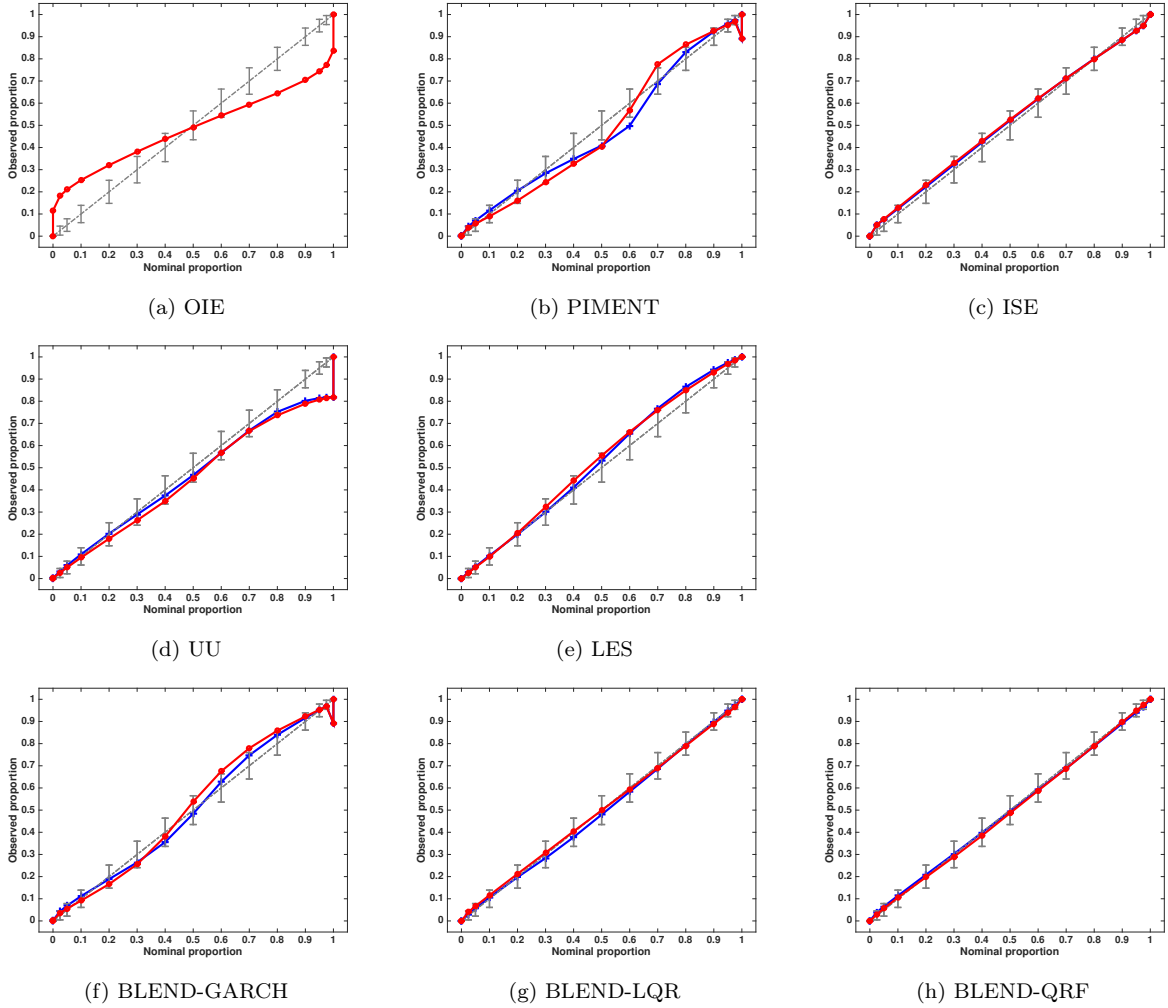


Figure 3: Reliability diagrams for all sites averaged over all the forecast horizons related to each participant. Consistency bars for a 90% confidence level around the ideal line are individually computed for each nominal proportion. The red curves stand for intra-hour forecasts while the blue one are for intra-day forecasts.

539 Irrespective of the scenario (intra-hour or intra-day), the visual analysis shows that
 540 only probabilistic forecasts derived from ISE (Figure 3c) possibly has a high reliability.
 541 All the other forecasts are possibly non reliable namely those generated by OIE (Figure
 542 3a), PIMENT (Figure 3b), UU (Figure 3d) and to a lesser extent LES (Figure 3e). More
 543 specifically, forecasts provided by OIE appear to be clearly non reliable and forecasts issued
 544 by LES, UU and PIMENT experience high deviations from the ideal line for high nominal
 545 proportions.

546 For the ISE forecasts for which the observed proportions lie within the consistency bars,
 547 while this does not confirm the perfect reliability of the quantile forecasts, it also does not
 548 allow us to confidently assert their lack of reliability at a 10% significance level.

549 *6.2. CRPS and its decomposition*

550 *6.2.1. Overall results for all sites*

551 Following Yang et al. (2020), Table 4 and Table 5 report the overall results (i.e. computed
 552 from the aggregation of forecasts and data of all sites) obtained by each metric in terms of
 553 “mean \pm standard deviation”. More precisely, for intra-hour forecasting, the mean and
 554 standard deviation are computed from the 8 values of the metric corresponding to the 8
 555 horizons while for intra-day forecasting, the mean and standard deviation are computed
 556 from the 16 values related to the 16 horizons (see Table 2). We recall here that intra-hour
 557 forecasts correspond to 15-120 min-ahead forecasting at 15mins timesteps while the intra-day
 558 forecasts are for 120-360 min-ahead forecasting at 15mins timesteps. Also, in this section,
 559 we will comment on the results obtained by the five participants with their original proposed
 560 method (see Table 1). The methods BLEND-GARCH, BLEND-LQR and BLEND-QRF will
 561 be presented and discussed later in Section 7.

562 Regarding intra-hour forecasts (see Table 4), the best performer is ISE regardless of the
 563 metric while the worst one is PIMENT. In terms of skill score, the forecast skill of ISE is (in
 564 average) 46.6% while PIMENT exhibits a skill score of 32.9%. It appears clearly that the
 565 better performance of ISE originates from its better resolution and reliability. In line with
 566 the reliability diagrams of Figure 3a, the CMV-based probabilistic method of OIE leads to
 567 poor results notably in terms of reliability. More generally, the quantitative reliability (REL)
 568 component of the CRPS confirms the visual diagnosis provided by the reliability diagrams
 569 in Figure 3. Finally, it should be noted that the linear LQR method proposed by LES, fed
 570 with ground and satellite data, achieves similar results to the nonlinear QRF method of UU,
 571 which uses only ground data.

572 As shown by Table 5, for intra-day forecasts, the same comments made above for intra-
 573 hour forecasts still hold. However, except for ISE, the only participant integrating NWP
 574 forecasts, one can observe a strong decrease in forecast skill particularly for PIMENT for
 575 which a decrease of 25 points in the mean skill score is noted. Similar to deterministic
 576 forecasts (see Figure 2), with increasing forecast horizon, the positive impact of integrating
 577 NWP forecasts in the modelling process is clearly demonstrated.

Method	CRPS (W/m ²)	CRPSS (%)	REL (W/m ²)	RES (W/m ²)	MAE (W/m ²)
OIE	53.8 \pm 5.6	34.6 \pm 6.7	4.5 \pm 0.3	101.8 \pm 5.4	67.9 \pm 8.3
PIMENT	55.2 \pm 10.3	32.9 \pm 12.5	3.9 \pm 0.7	99.7 \pm 9.6	72.9 \pm 15.4
ISE	43.9 \pm 6.6	46.6 \pm 8.1	0.8 \pm 0.2	107.9 \pm 6.5	59.4 \pm 9.4
UU	48.3 \pm 8.4	41.3 \pm 10.2	1.1 \pm 0.2	103.8 \pm 8.3	64.1 \pm 12.2
LES	47.1 \pm 8.6	42.8 \pm 10.4	1.5 \pm 0.3	105.5 \pm 8.3	62.7 \pm 12.1
BLEND-GARCH	47.7 \pm 6.9	42.1 \pm 8.3	2.0 \pm 0.3	105.4 \pm 6.6	61.6 \pm 9.2
BLEND-LQR	47.3 \pm 6.4	42.6 \pm 7.8	2.1 \pm 0.2	105.9 \pm 6.2	61.4 \pm 9.2
BLEND-QRF	44.2 \pm 5.9	46.3 \pm 7.2	1.1 \pm 0.1	107.9 \pm 5.8	59.5 \pm 8.6

Table 4: Intra-hour forecasts overall results. For each method, the metrics are presented as “mean \pm standard deviation,” calculated over all forecast horizons. For these overall results, the CRPS of the CSD-CLIM is 82.3 W.m⁻² and the uncertainty component UNC of the CRPS is 150.8 W.m⁻²

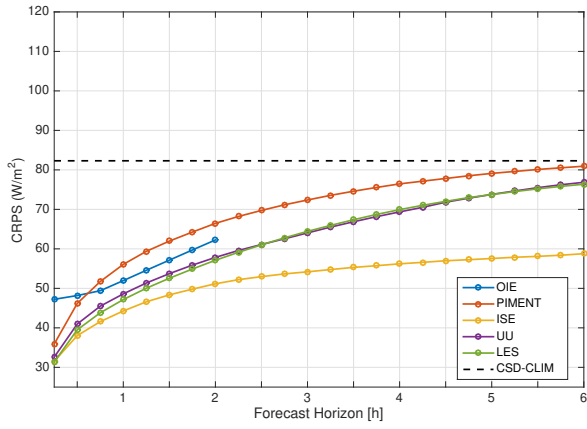
Method	CRPS (W/m^2)	CRPSS (%)	REL (W/m^2)	RES (W/m^2)	MAE (W/m^2)
OIE	NA	NA	NA	NA	NA
PIMENT	76.0 ± 4.0	7.7 ± 4.9	4.7 ± 0.1	79.8 ± 3.9	105.3 ± 6.5
ISE	56.0 ± 2.0	31.9 ± 2.5	1.3 ± 0.2	96.3 ± 1.9	76.6 ± 2.7
UU	69.3 ± 5.6	15.8 ± 6.8	1.6 ± 0.2	83.3 ± 5.4	96.3 ± 8.9
LES	69.4 ± 5.5	15.6 ± 6.7	2.7 ± 0.4	84.3 ± 5.1	94.5 ± 8.3
BLEND-GARCH	60.4 ± 2.2	26.6 ± 2.6	2.9 ± 0.3	93.6 ± 1.8	79.4 ± 3.0
BLEND-LQR	59.2 ± 2.0	28.0 ± 2.4	3.1 ± 0.4	94.9 ± 1.6	79.1 ± 2.9
BLEND-QRF	55.5 ± 2.0	32.5 ± 2.5	1.7 ± 0.2	97.2 ± 1.8	75.7 ± 2.8

Table 5: Intra-day forecasts overall results. For each method, the metrics are presented as “mean \pm standard deviation,” calculated over all forecast horizons. OIE has "NA" values since OIE method is limited to intra-hour forecasting.

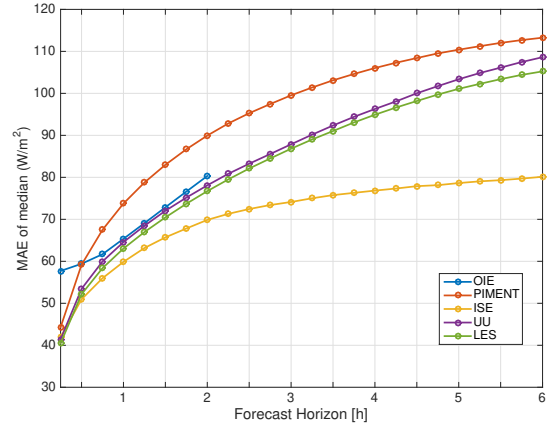
578 We complement the above quantitative metrics analysis summarized for intra-day and
579 day-ahead by plotting over all the forecast horizons the numerical scores selected for this
580 benchmarking exercise namely CRPS, CRPS reliability, CRPS resolution, MAE and CRPS
581 skill score (see Figure 4). It should also be noted that we deliberately use the same Y-scale
582 for the CRPS and MAE plots to emphasize the improvement in quality brought by the
583 probabilistic approach. Indeed, as shown by Figures 4a and 4b, the CRPS (i.e., the MAE)
584 of the median of the predictive distribution is clearly worse than the CRPS of the entire
585 predictive distribution.

586 As shown by all the plots, the highest overall skill of the ISE forecasts is clearly demon-
587 strated irrespective of the forecast horizon. In terms of CRPS skill score, over the whole
588 range of forecast horizons, the best performer is ISE with skill scores between 60% and
589 almost 30% while PIMENT forecasts lead to the worst forecasting results with a CRPS skill
590 score ranging between 55% and almost 0%

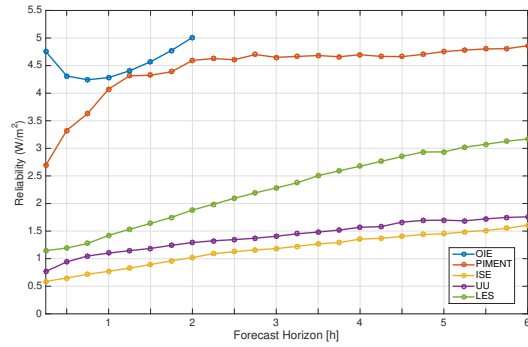
591 Again, the specific method developed by OIE does not outperform the other methods.
592 The forecasts issued by this technique are clearly non reliable and confirms the visual in-
593 spection of the related reliability diagram.



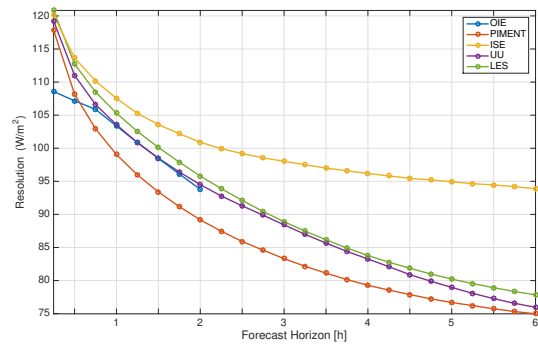
(a) CRPS



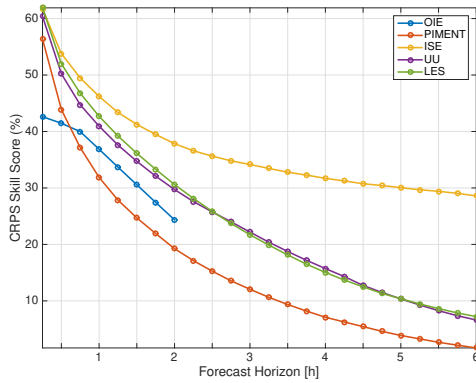
(b) MAE



(c) Reliability (REL)



(d) Resolution (RES)



(e) CRPS skill score

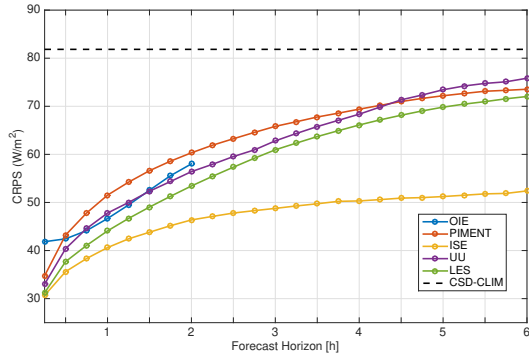
Figure 4: CRPS and its associated decomposition for all stations. Average GHI for all sites is $382.4 \text{ W}\cdot\text{m}^{-2}$ and can be used to calculate the relative counterparts of the different metrics. Notice that the same Y-scale is used for the CRPS and MAE plots to highlight the improvement brought by the probabilistic approach.

594 *6.2.2. Results for each site*

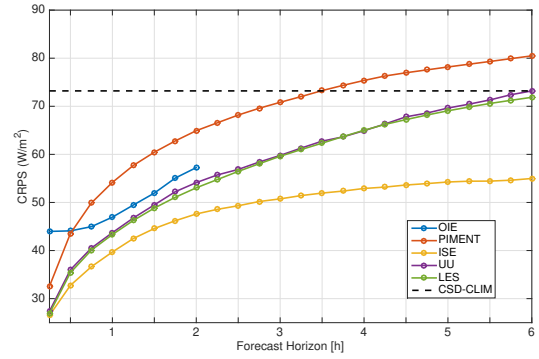
595 To gain a deeper insight in the performances of the different methods, Figure 5 focuses
 596 on the CRPS values obtained by each contestant for each of the eight sites. As shown,

597 again, the best CRPS values are obtained by ISE whatever the location. Interestingly, the
598 parametric model of PIMENT cannot beat the climatological model CSD-CLIM for some
599 sites namely CAR, MIL and TAB for certain forecast horizons.

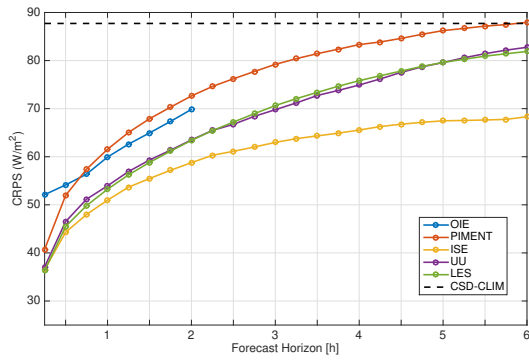
600 For the site TAB which is located in the South of Spain and corresponds to a semi-arid
601 climate (see Koppen-Geiger classification provided in Table 3) and which experiences a high
602 share of clear skies PIMENT is outperformed by CSD-CLIM at 1h lead time while at 2h
603 lead time, this is the case of LES and UU methods. Notice again the similar CRPS behavior
604 of LES and UU models.



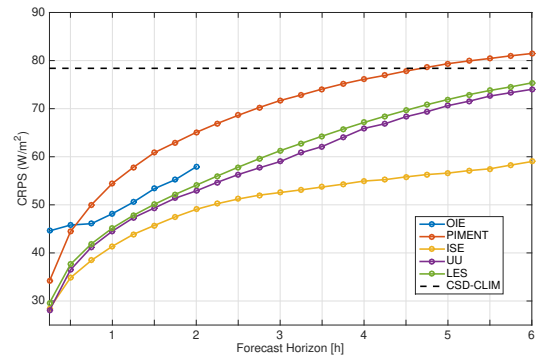
(a) CAB



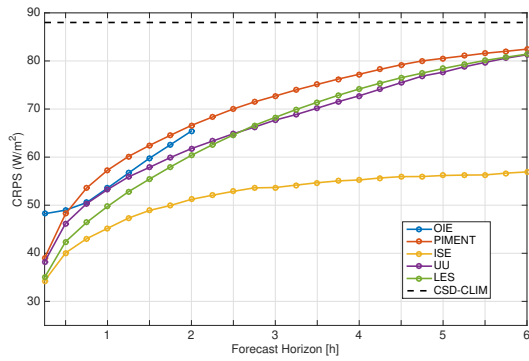
(b) CAR



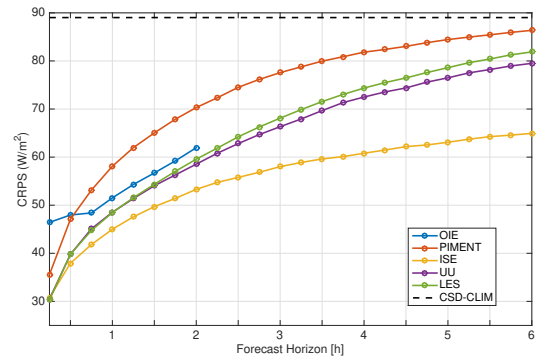
(c) CEN



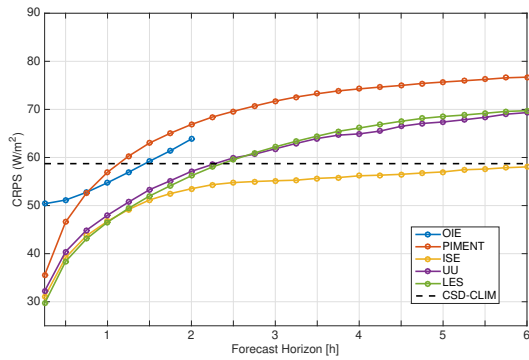
(d) MIL



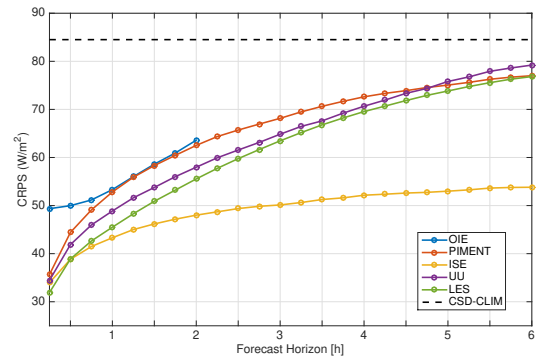
(e) PAL



(f) PAY



(g) TAB



(h) TOR

Figure 5: CRPS for the different locations. Table 3 lists the average GHI of each site that can be used to compute the relative CRPS

605 Finally, the interested reader is directed to Appendix 10 where results related to the 8
606 sites are tabulated.

607 **7. Impact of a high quality point forecast on the skills of the probabilistic meth-** 608 **ods**

609 In the previous Section 6, we observed that the ISE forecasting methodology clearly
610 outperforms the other methods. We hypothesize that the skill of the ISE method comes
611 from the blended point forecasts which are used by the Analog Ensemble technique and not
612 necessarily by the Analog technique by itself.

Method	Forecasting technology	Input data
BLEND-GARCH	ISE blended point fcst + GARCH	ground data+SAT+NWP
BLEND-LQR	ISE blended point fcst + LQR technique	ground data+SAT+NWP
BLEND-QRF	ISE blended point fcst + QRF technique	ground data+SAT+NWP

Table 6: New proposed forecasting methods

613 In order to confirm our assumption, we use the same blended point forecasts as inputs to
614 three other approaches to generate probabilistic forecasts, including the PIMENT parametric
615 GARCH approach, applied to ARMA point forecasts before. This new forecast is denoted
616 BLEND-GARCH. In addition, we designed two other models based respectively on the
617 LQR and QRF technique that use as input the blended ISE forecasts. These 2 new models
618 are denoted BLEND-LQR and BLEND-QRF. Table 6 lists the new combinations of the
619 ISE blended point forecast with the different techniques employed to generate the quantile
620 forecasts. The results of the newly proposed methods are listed in the last 3 lines of Table
621 4 and Table 5.

622 The combination BLEND-GARCH clearly improves the original PIMENT method for
623 all the considered metrics. In particular, for the intra-hour scenario, the gain in average skill
624 score is 9 points while for intra-day forecast, the gain in average forecast skill is 19 points.
625 The decomposition of the CRPS permits to highlight the improvement in resolution brought
626 by the BLEND-GARCH combination.

627 Regardless of the scenario (intra-hour or intra-day forecasts), we can state that the
628 BLEND-GARCH and BLEND-LQR exhibit similar performances. The same statement is
629 also valid for BLEND-QRF and ISE forecasts.

630 Specifically, for intra-day forecasts, the BLEND-QRF slightly outperforms the original
631 ISE method in terms of forecast skill.

632 Again, for a better inspection of the results, we provide the visual display of the metrics.
633 Here also, in Figure 6 the metrics are computed from the aggregation of forecasts and GHI
634 data of all sites while Figure 7 plots the CRPS obtained on each site. Notice that, for sake of
635 comparison, the metrics related to the ISE and PIMENT previous methods are also plotted.

636 As shown by Figure 6, irrespective of the forecast horizon and metric, a clear improvement
637 is brought by using the blended point forecasts. For instance, Figure 6e shows that the CRPS

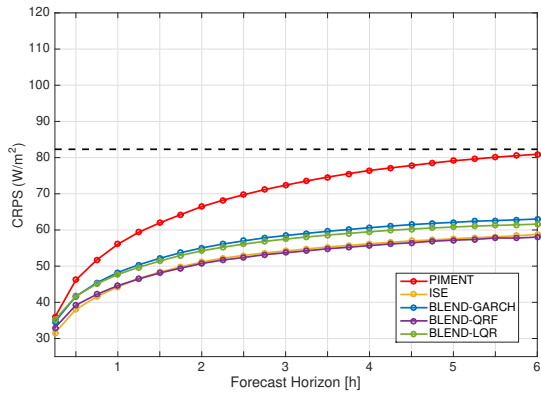
638 skill score of the new BLEND-GARCH now ranges from 58% to 22% instead of 56% to 1%
639 obtained by the previous PIMENT method. The improvement is more pronounced at higher
640 forecasting horizons and at the last forecast horizon the skill score of the previous PIMENT
641 method based on ground measurements only is increased by almost 22 percentage points.

642 Also, combining the blended forecasts with techniques like LQR or QRF improves the
643 skills of the probabilistic forecasts. From the decomposition of the CRPS into REL and
644 RES, it appears that the BLEND-QRF slightly outperforms the ISE method in terms of
645 resolution. However, the ISE method is still the best performer in terms of reliability.

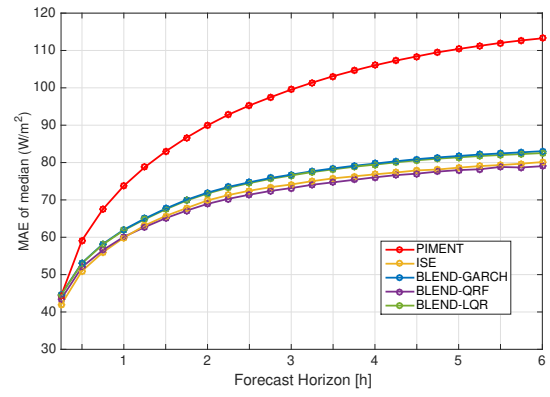
646 Figure 7 displays the CRPS obtained by the new combinations for each site under study.
647 Now, all the new proposed forecasting techniques beat the CSD-CLIM model but for the site
648 TAB (see Figure 7g) the CSD-CLIM outperforms the BLEND-GARCH from a 2h forecast
649 horizon. Note that for the site TAB, the BLEND-QRF exhibits the best skill, a considerable
650 improvement compared to the Analog Ensemble is found from two hour on-wards.

651 From the previous results, we can conclude that the use of the blended point forecasts
652 of participant ISE improves substantially the PIMENT parametric approach forecasting
653 models. Further, the improvements are slightly better when the blended point forecasts are
654 inputted to a nonlinear machine learning technique such as QRF.

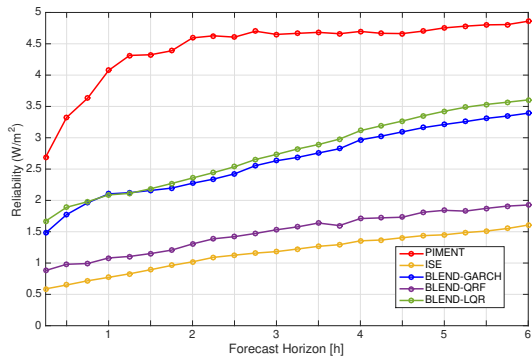
655 In terms of reliability diagrams, the situation is also clearly improved when one compares
656 Figure 3f against 3b albeit it seems that BLEND-GARCH intra-hour forecasts still suffer
657 from a lack of reliability at high nominal proportions. Moreover, Figures 3g and 3h reveal
658 that the new proposed method BLEND-LQR and BLEND-QRF generate reliable forecasts.



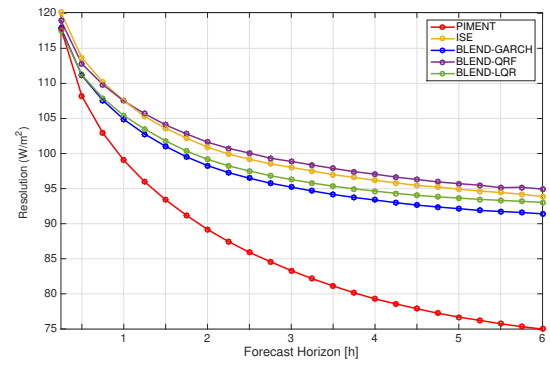
(a) CRPS



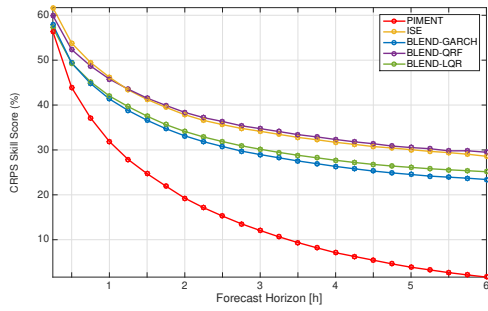
(b) MAE



(c) Reliability (REL)

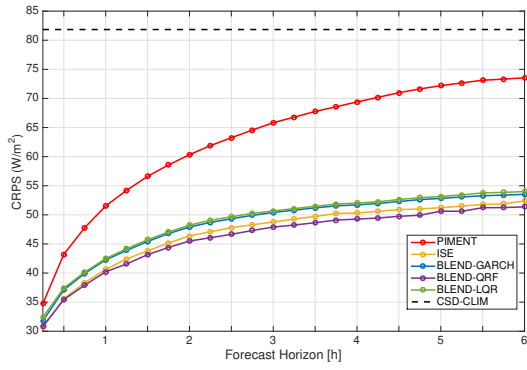


(d) Resolution (RES)

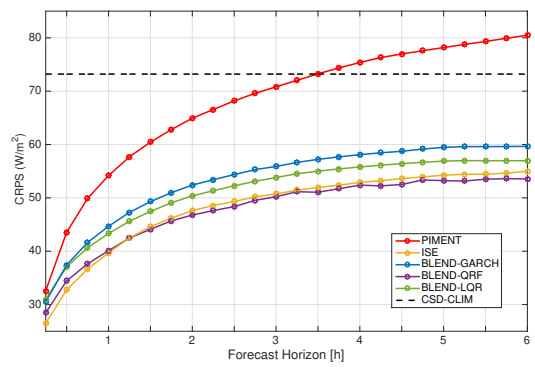


(e) CRPS skill score

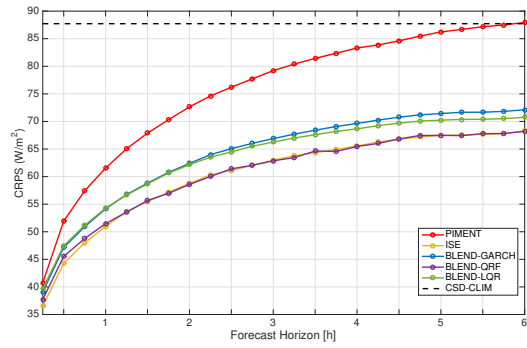
Figure 6: CRPS and its associated decomposition for all stations and for the new proposed models



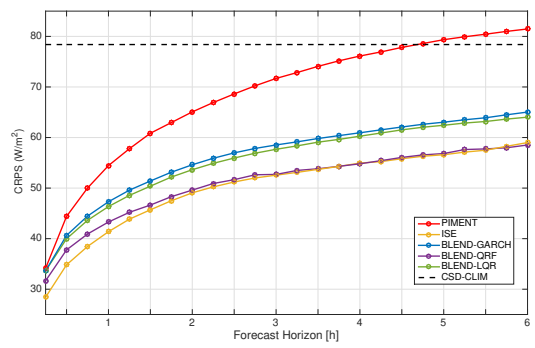
(a) CAB



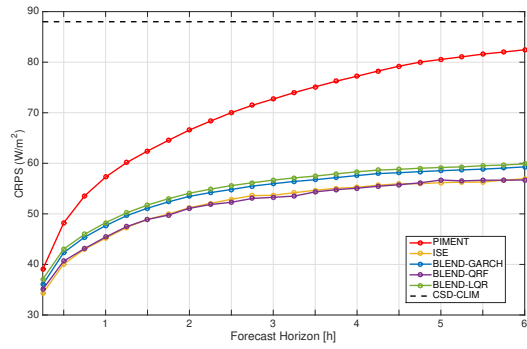
(b) CAR



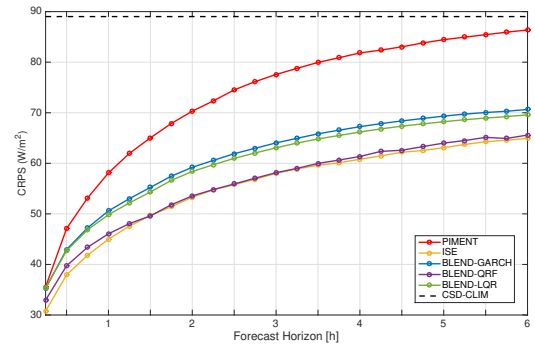
(c) CEN



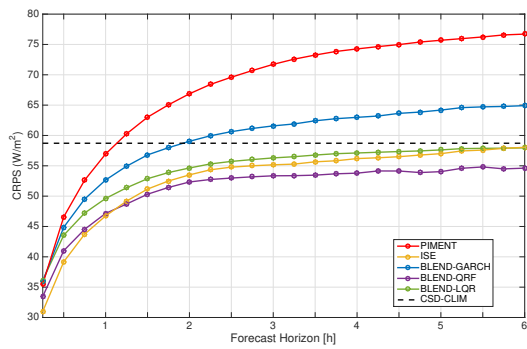
(d) MIL



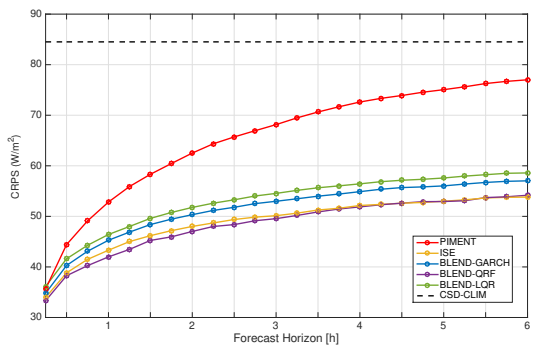
(e) PAL



(f) PAY



(g) TAB



(h) TOR

Figure 7: Improved CRPS by using the blending deterministic forecasts of Fraunhofer ISE for the different locations.

659 8. Summary and conclusion

660 A benchmarking procedure set up by a group of experts of the IEA PVPS Task 16 was
661 implemented to assess the performance of intra-hour and intra-day probabilistic solar irradi-
662 ance forecasts. This procedure was utilized to evaluate eight distinct forecasting algorithms.

663 In the initial stage, the benchmarking exercise involved evaluating probabilistic forecasts
664 submitted directly by five different participants. This initial comparison of forecasts using
665 different input data and methods revealed a significant variation in performance. Partic-
666 ularly, during this first step, a probabilistic forecast that utilized a blended point forecast
667 outperformed the other methods. In a second analysis, to better understand the impact of
668 input data versus methodology on forecast quality, we combined the well-performing blended
669 point forecast from the first comparison with different probabilistic approaches.

670 As mentioned earlier, the first stage of this work revealed that the initially proposed
671 methods exhibit varying levels of forecast quality. In particular, the satellite-based method
672 recently developed by OIE, which directly generates the set of quantile forecasts from a CMV
673 model, suffers from a lack of reliability that significantly impacts its overall performance.
674 However, a calibration technique could be employed to enhance this attribute. As expected,
675 a parametric approach, like the one proposed by PIMENT is not suitable to provide high
676 quality probabilistic solar forecast, even with the high performing point forecast as input.

677 The second stage of this study demonstrated that a high quality point forecast (that
678 blends measurements, satellite-based and NWP forecasts) used in combination with a sta-
679 tistical technique is able to generate probabilistic forecasts with high quality. Overall, the
680 skill scores of methods employing the blended point forecast vary between 42% and 46% for
681 the intra-hour scenario and between 27% and 32% for the intra-day scenario. In contrast,
682 methods that do not utilize the blended point forecast but are based on measurements and/or
683 satellite data only exhibit skill scores ranging from 33% to 43% for intra-hour forecasts and
684 from 8% to 16% for intra-day forecasts.

685 Besides a good forecast skill, the methodology that consists in generating probabilistic
686 forecasts in a two step approach has the advantage that it is easy to implement in combina-
687 tion with blended deterministic forecasts that are well understood and used operationally. It
688 allows to benefit from high quality deterministic point forecasts with comparatively simple
689 probabilistic techniques applied in a post-processing step.

690 An alternative to blending the deterministic forecasts before applying the probabilistic
691 techniques, would be to directly use the three deterministic forecasts as input to these
692 techniques. LQR or QRF can be applied to generate quantile forecasts from different inputs
693 in one step. For the AnEn method the different inputs can be combined with predictor
694 weighting. Setting up these more complex models will be subject of future investigations.

695 Ongoing efforts by members of the IEA PVPS Task 16 involve the continuing develop-
696 ment of solar probabilistic methods. Consequently, the evaluation and comparison of prob-
697 abilistic forecasts will persist, and further analysis will be conducted using recent ground
698 measurement data, satellite or NWP data. This continuing research aims to enhance the
699 quality of solar irradiance probabilistic forecasts.

700 **9. ACKNOWLEDGEMENTS**

701 This research paper contributes to the IEA PVPS task 16 "Task 16 Solar resource for
 702 high penetration and large-scale applications," which is a collaborative effort between the
 703 International Energy Agency's. The study also received support from the TwInSolar project
 704 funded by the European Union's Horizon Europe research and innovation program grant
 705 number 101076447.

706 R. Alonso-Suárez acknowledges financial support from the CSIC Group's Program, Uni-
 707 versidad de la República, Uruguay.

708 The research contribution of Tobias Zech, Wiebke Herzberg, Elke Lorenz (Fraunhofer
 709 ISE) received funding by the German Federal Ministry for Economic Affairs and Climate
 710 Action (BMWK) within the SOLREV project (Grant Agreement no. 03EE1010) on the
 711 basis of a decision by the German Bundestag.

712 The authors express their gratitude to Anna Forstinger for providing the ground datasets.

713 **10. Appendices**

714 **Appendix A Intra-hour and intra-day forecasts results site CAB**

Method	CRPS (W/m^2)	CRPSS (%)	REL (W/m^2)	RES (W/m^2)	MAE (W/m^2)
OIE	48.8 ± 6.1	40.3 ± 7.5	4.7 ± 0.4	81.8 ± 5.7	61.1 ± 8.5
PIMENT	50.9 ± 8.6	37.8 ± 10.5	2.1 ± 0.2	77.1 ± 8.4	69.2 ± 13.2
ISE	40.4 ± 5.3	50.7 ± 6.5	0.9 ± 0.2	86.4 ± 5.1	55.4 ± 7.6
UU	47.4 ± 7.8	42.1 ± 9.5	1.8 ± 0.4	80.3 ± 7.4	63.7 ± 11.4
LES	44.3 ± 7.4	45.9 ± 9.1	1.7 ± 0.5	83.2 ± 7.0	59.8 ± 10.2
BLEND-GARCH	41.9 ± 5.4	48.8 ± 6.6	1.9 ± 0.3	85.8 ± 5.1	55.0 ± 7.6
BLEND-LQR	42.2 ± 5.3	48.4 ± 6.5	2.1 ± 0.4	85.7 ± 4.9	54.7 ± 7.3
BLEND-QRF	39.9 ± 4.9	51.3 ± 6.0	1.1 ± 0.2	87.0 ± 4.7	54.3 ± 7.0

Table 7: Same as for Table 4 (intra-hour) but for site CAB. For site CAB, the CRPS of the CSD-CLIM is $81.8 W.m^{-2}$ and the uncertainty component UNC of the CRPS is $125.9 W.m^{-2}$.

Method	CRPS (W/m^2)	CRPSS (%)	REL (W/m^2)	RES (W/m^2)	MAE (W/m^2)
OIE	NA	NA	NA	NA	NA
PIMENT	69.1 ± 3.8	15.6 ± 4.6	2.4 ± 0.2	59.1 ± 3.6	98.2 ± 6.1
ISE	50.2 ± 1.6	38.7 ± 1.9	1.0 ± 0.1	76.6 ± 1.6	69.4 ± 2.4
UU	68.4 ± 5.9	16.5 ± 7.2	3.7 ± 0.8	61.2 ± 5.1	96.3 ± 9.6
LES	65.6 ± 5.3	19.9 ± 6.4	3.7 ± 0.7	64.0 ± 4.6	89.8 ± 8.2
BLEND-GARCH	51.7 ± 1.5	36.9 ± 1.8	2.2 ± 0.1	76.4 ± 1.6	69.5 ± 2.2
BLEND-QRF	49.2 ± 1.6	39.9 ± 2.0	1.3 ± 0.1	78.0 ± 1.7	67.8 ± 2.5
BLEND-LQR	52.0 ± 1.5	36.5 ± 1.9	2.7 ± 0.0	76.6 ± 1.6	68.5 ± 2.4
BLEND-QRF	49.2 ± 1.6	39.9 ± 2.0	1.3 ± 0.1	78.0 ± 1.7	67.8 ± 2.5

Table 8: Same as for Table 5 (intra-day) but for site CAB

715 **Appendix B Intra-hour and intra-day forecasts results site CAR**

Method	CRPS	CRPSS	REL	RES	MAE
OIE	49.2 ± 5.1	32.8 ± 7.0	4.3 ± 0.4	108.5 ± 5.1	63.0 ± 7.4
PIMENT	53.3 ± 10.9	27.2 ± 14.9	5.3 ± 0.7	105.4 ± 10.2	68.8 ± 16.3
ISE	39.6 ± 7.2	46.0 ± 9.9	1.1 ± 0.3	114.9 ± 7.0	53.3 ± 10.0
UU	43.8 ± 8.9	40.2 ± 12.2	1.1 ± 0.2	110.7 ± 8.8	58.0 ± 12.9
LES	43.1 ± 8.7	41.1 ± 12.0	1.7 ± 0.3	112.0 ± 8.5	57.3 ± 12.6
BLEND-GARCH	44.3 ± 7.4	39.5 ± 10.2	2.9 ± 0.4	112.0 ± 7.0	55.8 ± 9.5
BLEND-LQR	43.1 ± 6.6	41.2 ± 9.0	2.9 ± 0.2	113.2 ± 6.3	55.0 ± 9.6
BLEND-QRF	40.0 ± 6.2	45.4 ± 8.5	1.3 ± 0.2	114.7 ± 6.1	53.2 ± 8.9

Table 9: Same as for Table 4 (intra-hour) but for site CAR. For site CAR, the CRPS of the CSD-CLIM is 73.2 W.m⁻² and the uncertainty component UNC of the CRPS is 152.3 W.m⁻².

Method	CRPS (W/m ²)	CRPSS (%)	REL (W/m ²)	RES (W/m ²)	MAE (W/m ²)
OIE	NA	NA	NA	NA	NA
PIMENT	74.9 ± 4.4	-2.3 ± 6.0	6.3 ± 0.2	84.9 ± 4.2	102.2 ± 7.0
ISE	52.6 ± 2.0	28.2 ± 2.7	1.8 ± 0.2	102.7 ± 1.8	71.0 ± 2.6
UU	65.2 ± 5.6	10.9 ± 7.7	1.3 ± 0.1	89.5 ± 5.7	90.8 ± 8.9
LES	64.7 ± 5.5	11.6 ± 7.5	2.5 ± 0.2	91.1 ± 5.3	88.1 ± 8.0
BLEND-GARCH	57.7 ± 2.0	21.2 ± 2.8	3.7 ± 0.2	99.4 ± 1.8	73.7 ± 2.4
BLEND-LQR	55.3 ± 1.8	24.4 ± 2.5	4.1 ± 0.4	102.2 ± 1.4	73.6 ± 2.6
BLEND-QRF	51.7 ± 1.9	29.4 ± 2.6	2.1 ± 0.3	103.8 ± 1.6	69.7 ± 2.6

Table 10: Same as for Table 5 (intra-day) but for site CAR

716 **Appendix C Intra-hour and intra-day forecasts results site CEN**

Method	CRPS (W/m ²)	CRPSS (%)	REL (W/m ²)	RES (W/m ²)	MAE (W/m ²)
OIE	60.9 ± 6.4	30.6 ± 7.3	5.5 ± 0.3	96.2 ± 6.5	78.4 ± 10.1
PIMENT	60.9 ± 10.6	30.5 ± 12.1	4.0 ± 0.7	94.6 ± 9.9	82.5 ± 16.2
ISE	50.6 ± 7.4	42.3 ± 8.5	1.0 ± 0.2	102.0 ± 7.2	69.4 ± 10.9
UU	53.7 ± 8.7	38.7 ± 9.9	0.9 ± 0.1	98.7 ± 8.6	73.1 ± 13.2
LES	53.1 ± 9.0	39.5 ± 10.2	1.2 ± 0.3	99.7 ± 8.7	72.2 ± 13.0
BLEND-GARCH	53.8 ± 7.8	38.7 ± 8.9	1.9 ± 0.3	99.7 ± 7.5	72.0 ± 11.0
BLEND-LQR	53.8 ± 7.5	38.6 ± 8.6	2.4 ± 0.5	100.1 ± 7.1	71.4 ± 11.3
BLEND-QRF	51.0 ± 6.9	41.8 ± 7.9	0.8 ± 0.1	101.4 ± 6.8	70.3 ± 10.4

Table 11: Same as for Table 4 (intra-hour) but for site CEN. For site CEN, the CRPS of the CSD-CLIM is 87.7 W.m⁻² and the uncertainty component UNC of the CRPS is 153.1 W.m⁻².

Method	CRPS (W/m^2)	CRPSS (%)	REL (W/m^2)	RES (W/m^2)	MAE (W/m^2)
OIE	NA	NA	NA	NA	NA
PIMENT	82.8 ± 4.2	5.6 ± 4.8	5.3 ± 0.1	74.1 ± 4.1	116.6 ± 6.6
ISE	65.2 ± 2.6	25.6 ± 2.9	1.7 ± 0.2	88.1 ± 2.4	90.6 ± 3.5
UU	75.1 ± 5.6	14.4 ± 6.4	0.8 ± 0.1	77.3 ± 5.7	107.9 ± 9.4
LES	75.4 ± 5.3	14.1 ± 6.0	2.1 ± 0.2	78.2 ± 5.0	105.8 ± 8.6
BLEND-GARCH	69.2 ± 2.6	21.1 ± 3.0	2.7 ± 0.2	85.0 ± 2.4	94.0 ± 3.5
BLEND-LQR	68.3 ± 2.3	22.2 ± 2.7	3.2 ± 0.2	86.5 ± 2.1	94.0 ± 3.7
BLEND-QRF	65.2 ± 2.6	25.7 ± 3.0	1.1 ± 0.1	87.4 ± 2.6	91.9 ± 3.9

Table 12: Same as for Table 5 (intra-day) but for site CEN

717 Appendix D Intra-hour and intra-day forecasts results site MIL

Method	CRPS (W/m^2)	CRPSS (%)	REL (W/m^2)	RES (W/m^2)	MAE (W/m^2)
OIE	50.2 ± 4.9	36.0 ± 6.2	4.2 ± 0.4	109.6 ± 4.6	63.8 ± 7.4
PIMENT	53.7 ± 10.5	31.5 ± 13.3	6.3 ± 1.1	108.2 ± 9.4	66.5 ± 15.2
ISE	41.1 ± 7.0	47.5 ± 8.9	1.4 ± 0.4	115.8 ± 6.6	54.6 ± 9.7
UU	43.9 ± 8.4	44.0 ± 10.7	0.9 ± 0.1	112.6 ± 8.3	58.3 ± 12.2
LES	44.8 ± 8.2	42.8 ± 10.4	3.8 ± 0.5	114.6 ± 7.7	56.1 ± 11.3
BLEND-GARCH	46.8 ± 7.0	40.2 ± 9.0	4.3 ± 0.6	113.1 ± 6.4	57.2 ± 9.2
BLEND-LQR	46.0 ± 6.7	41.3 ± 8.6	4.4 ± 0.8	114.0 ± 5.9	58.8 ± 9.3
BLEND-QRF	42.9 ± 6.0	45.2 ± 7.6	2.6 ± 0.5	115.3 ± 5.5	56.3 ± 8.2

Table 13: Same as for Table 4 (intra-hour) but for site MIL. For site MIL, the CRPS of the CSD-CLIM is $78.4 W.m^{-2}$ and the uncertainty component UNC of the CRPS is $154.6 W.m^{-2}$.

Method	CRPS (W/m^2)	CRPSS (%)	REL (W/m^2)	RES (W/m^2)	MAE (W/m^2)
OIE	NA	NA	NA	NA	NA
PIMENT	75.7 ± 4.6	3.4 ± 5.8	7.8 ± 0.1	87.8 ± 4.5	100.2 ± 7.2
ISE	54.9 ± 2.6	30.0 ± 3.3	3.2 ± 0.6	104.0 ± 2.0	73.4 ± 3.2
UU	65.4 ± 6.4	16.5 ± 8.2	0.9 ± 0.1	91.1 ± 6.3	91.0 ± 10.0
LES	67.0 ± 6.2	14.5 ± 7.9	5.5 ± 0.6	94.1 ± 5.6	86.5 ± 9.0
BLEND-GARCH	61.0 ± 2.8	22.2 ± 3.5	6.5 ± 0.7	101.1 ± 2.1	77.4 ± 4.3
BLEND-LQR	60.2 ± 2.8	23.2 ± 3.6	8.0 ± 1.3	103.4 ± 1.6	79.9 ± 4.6
BLEND-QRF	55.1 ± 2.4	29.8 ± 3.0	4.3 ± 0.4	104.8 ± 2.0	72.7 ± 3.1

Table 14: Same as for Table 5 (intra-day) but for site MIL

718 **Appendix E Intra-hour and intra-day forecasts results site PAL**

Method	CRPS (W/m^2)	CRPSS (%)	REL (W/m^2)	RES (W/m^2)	MAE (W/m^2)
OIE	55.7 ± 6.5	36.7 ± 7.3	5.3 ± 0.5	92.4 ± 6.0	69.3 ± 9.1
PIMENT	56.5 ± 9.2	35.8 ± 10.5	2.9 ± 0.4	89.3 ± 8.9	76.9 ± 14.3
ISE	45.0 ± 5.7	48.9 ± 6.5	1.2 ± 0.2	99.0 ± 5.5	61.3 ± 8.2
UU	52.9 ± 7.8	39.9 ± 8.9	2.0 ± 0.3	92.0 ± 7.6	70.3 ± 11.6
LES	50.0 ± 8.5	43.2 ± 9.6	1.7 ± 0.4	94.6 ± 8.1	68.0 ± 11.9
BLEND-GARCH	47.3 ± 5.8	46.3 ± 6.6	1.8 ± 0.2	97.4 ± 5.7	62.3 ± 8.1
BLEND-LQR	47.9 ± 5.7	45.5 ± 6.5	2.2 ± 0.3	97.1 ± 5.4	62.2 ± 8.1
BLEND-QRF	45.2 ± 5.4	48.6 ± 6.1	1.3 ± 0.2	98.9 ± 5.2	61.4 ± 7.8

Table 15: Same as for Table 4 (intra-hour) but for site PAL. For site PAL, the CRPS of the CSD-CLIM is $88.0 W.m^{-2}$ and the uncertainty component UNC of the CRPS is $140.5 W.m^{-2}$.

Method	CRPS (W/m^2)	CRPSS (%)	REL (W/m^2)	RES (W/m^2)	MAE (W/m^2)
OIE	NA	NA	NA	NA	NA
PIMENT	76.9 ± 4.5	12.6 ± 5.1	3.6 ± 0.2	69.6 ± 4.3	109.4 ± 7.3
ISE	55.1 ± 1.4	37.4 ± 1.6	1.4 ± 0.1	89.2 ± 1.5	75.9 ± 2.0
UU	73.1 ± 5.8	16.9 ± 6.6	2.7 ± 0.3	72.5 ± 5.5	102.6 ± 9.8
LES	73.7 ± 6.0	16.2 ± 6.8	3.4 ± 0.6	72.5 ± 5.4	102.3 ± 9.4
BLEND-GARCH	57.3 ± 1.6	34.9 ± 1.8	2.2 ± 0.2	87.8 ± 1.4	76.9 ± 2.3
BLEND-LQR	58.0 ± 1.5	34.1 ± 1.8	3.2 ± 0.3	88.0 ± 1.2	76.9 ± 2.3
BLEND-QRF	54.9 ± 1.7	37.6 ± 1.9	1.8 ± 0.2	89.7 ± 1.5	75.4 ± 2.3

Table 16: Same as for Table 5 (intra-day) but for site PAL

719 **Appendix F Intra-hour and intra-day forecasts results site PAY**

Method	CRPS (W/m^2)	CRPSS (%)	REL (W/m^2)	RES (W/m^2)	MAE (W/m^2)
OIE	53.3 ± 5.7	40.1 ± 6.4	4.7 ± 0.3	105.3 ± 5.8	68.4 ± 9.0
PIMENT	57.4 ± 11.7	35.5 ± 13.1	4.6 ± 0.6	101.2 ± 11.1	75.2 ± 17.7
ISE	44.7 ± 7.6	49.8 ± 8.5	0.9 ± 0.1	110.1 ± 7.4	61.1 ± 11.0
UU	48.0 ± 9.3	46.1 ± 10.5	1.3 ± 0.3	107.2 ± 9.1	64.0 ± 13.3
LES	48.2 ± 9.7	45.8 ± 10.9	2.0 ± 0.5	107.7 ± 9.2	64.3 ± 13.8
BLEND-GARCH	50.1 ± 8.0	43.7 ± 9.0	3.0 ± 0.3	106.8 ± 7.8	64.9 ± 11.2
BLEND-LQR	49.5 ± 7.7	44.4 ± 8.6	3.4 ± 0.6	107.8 ± 7.1	64.6 ± 11.2
BLEND-QRF	45.6 ± 6.8	48.7 ± 7.6	1.8 ± 0.2	110.1 ± 6.6	61.7 ± 10.1

Table 17: Same as for Table 4 (intra-hour) but for site PAY. For site PAY, the CRPS of the CSD-CLIM is $89.0 W.m^{-2}$ and the uncertainty component UNC of the CRPS is $151.6 W.m^{-2}$.

Method	CRPS (W/m^2)	CRPSS (%)	REL (W/m^2)	RES (W/m^2)	MAE (W/m^2)
OIE	NA	NA	NA	NA	NA
PIMENT	81.1 ± 4.3	8.8 ± 4.8	5.5 ± 0.1	78.2 ± 4.2	112.0 ± 6.7
ISE	60.7 ± 3.2	31.8 ± 3.6	1.4 ± 0.2	94.6 ± 3.0	84.7 ± 4.5
UU	71.9 ± 6.0	19.2 ± 6.7	1.9 ± 0.2	83.9 ± 5.8	100.0 ± 9.4
LES	73.8 ± 6.3	17.1 ± 7.1	4.6 ± 1.1	84.7 ± 5.2	101.2 ± 9.4
BLEND-GARCH	66.8 ± 3.2	24.9 ± 3.6	4.1 ± 0.4	91.2 ± 2.8	88.4 ± 4.3
BLEND-LQR	65.8 ± 3.1	26.1 ± 3.5	5.4 ± 0.6	93.5 ± 2.5	88.4 ± 4.4
BLEND-QRF	61.2 ± 3.4	31.2 ± 3.9	2.7 ± 0.3	95.4 ± 3.2	84.3 ± 4.8

Table 18: Same as for Table 5 (intra-day) but for site PAY

720 Appendix G Intra-hour and intra-day forecasts results site TAB

Method	CRPS (W/m^2)	CRPSS (%)	REL (W/m^2)	RES (W/m^2)	MAE (W/m^2)
OIE	56.3 ± 4.9	4.1 ± 8.4	6.2 ± 0.8	111.3 ± 4.2	70.2 ± 7.1
PIMENT	55.9 ± 10.6	4.9 ± 18.1	6.0 ± 1.2	111.5 ± 9.5	72.7 ± 16.0
ISE	45.9 ± 7.7	21.9 ± 13.1	1.6 ± 0.5	117.2 ± 7.2	59.9 ± 10.5
UU	47.7 ± 8.3	18.7 ± 14.2	1.4 ± 0.3	115.1 ± 8.0	61.2 ± 11.5
LES	46.2 ± 8.9	21.4 ± 15.1	1.2 ± 0.2	116.4 ± 8.7	61.2 ± 12.6
BLEND-GARCH	51.5 ± 7.8	12.3 ± 13.3	3.7 ± 0.9	113.7 ± 6.9	63.9 ± 9.6
BLEND-LQR	48.7 ± 6.3	17.1 ± 10.7	3.1 ± 0.3	115.8 ± 6.0	63.6 ± 9.1
BLEND-QRF	46.1 ± 6.3	21.5 ± 10.8	1.6 ± 0.3	116.9 ± 6.1	60.5 ± 8.8

Table 19: Same as for Table 4 (intra-hour) but for site TAB. For site TAB, the CRPS of the CSD-CLIM is $58.7 W.m^{-2}$ and the uncertainty component UNC of the CRPS is $160.0 W.m^{-2}$.

Method	CRPS (W/m^2)	CRPSS (%)	REL (W/m^2)	RES (W/m^2)	MAE (W/m^2)
OIE	NA	NA	NA	NA	NA
PIMENT	73.8 ± 2.6	-25.7 ± 4.3	7.8 ± 0.4	95.5 ± 2.2	101.2 ± 4.2
ISE	56.2 ± 1.2	4.2 ± 2.0	3.4 ± 0.6	108.6 ± 0.5	73.9 ± 1.2
UU	64.9 ± 3.3	-10.5 ± 5.7	1.7 ± 0.1	98.2 ± 3.4	84.1 ± 4.2
LES	65.5 ± 3.7	-11.6 ± 6.4	2.1 ± 0.3	98.0 ± 3.4	87.4 ± 4.6
BLEND-GARCH	63.0 ± 1.6	-7.2 ± 2.7	6.4 ± 0.9	104.9 ± 0.7	80.1 ± 2.5
BLEND-LQR	57.0 ± 0.8	2.9 ± 1.4	4.1 ± 0.5	108.5 ± 0.4	76.6 ± 1.3
BLEND-QRF	53.8 ± 0.6	8.3 ± 1.1	2.3 ± 0.2	109.9 ± 0.5	71.7 ± 0.8

Table 20: Same as for Table 5 (intra-day) but for site TAB

721 **Appendix H Intra-hour and intra-day forecasts results site TOR**

Method	CRPS (W/m^2)	CRPSS (%)	REL (W/m^2)	RES (W/m^2)	MAE (W/m^2)
OIE	55.4 ± 5.3	34.5 ± 6.3	7.3 ± 0.4	79.9 ± 4.9	67.3 ± 7.6
PIMENT	52.4 ± 9.0	38.0 ± 10.7	2.6 ± 0.2	78.1 ± 8.8	70.0 ± 13.4
ISE	43.0 ± 4.8	49.1 ± 5.6	0.9 ± 0.0	85.8 ± 4.8	59.3 ± 7.0
UU	48.8 ± 7.8	42.2 ± 9.3	2.3 ± 0.6	81.4 ± 7.3	64.4 ± 11.4
LES	45.9 ± 7.9	45.7 ± 9.3	1.7 ± 0.5	83.7 ± 7.4	62.1 ± 10.7
BLEND-GARCH	44.8 ± 5.2	47.0 ± 6.2	1.7 ± 0.1	84.8 ± 5.1	60.0 ± 7.2
BLEND-LQR	46.1 ± 5.2	45.5 ± 6.2	2.8 ± 0.4	84.7 ± 4.9	59.4 ± 7.3
BLEND-QRF	41.9 ± 4.6	50.4 ± 5.4	1.4 ± 0.1	87.4 ± 4.5	56.9 ± 6.9

Table 21: Same as for Table 4 (intra-hour) but for site TOR. For site TOR, the CRPS of the CSD-CLIM is $84.5 W.m^{-2}$ and the uncertainty component UNC of the CRPS is $125.9 W.m^{-2}$.

Method	CRPS (W/m^2)	CRPSS (%)	REL (W/m^2)	RES (W/m^2)	MAE (W/m^2)
OIE	NA	NA	NA	NA	NA
PIMENT	72.0 ± 4.1	14.8 ± 4.8	2.8 ± 0.1	58.8 ± 4.0	100.9 ± 6.8
ISE	51.8 ± 1.6	38.7 ± 1.9	1.1 ± 0.1	77.2 ± 1.6	72.0 ± 2.3
UU	70.7 ± 6.3	16.3 ± 7.4	5.1 ± 1.0	62.3 ± 5.3	98.3 ± 10.9
LES	69.1 ± 6.1	18.3 ± 7.2	4.6 ± 1.0	63.5 ± 5.1	93.7 ± 9.4
BLEND-GARCH	54.7 ± 1.9	35.3 ± 2.2	2.5 ± 0.3	75.7 ± 1.6	72.6 ± 2.3
BLEND-LQR	56.2 ± 1.9	33.4 ± 2.2	4.2 ± 0.4	75.9 ± 1.5	72.4 ± 2.2
BLEND-QRF	51.6 ± 2.0	39.0 ± 2.4	2.2 ± 0.2	78.5 ± 1.8	70.2 ± 2.6

Table 22: Same as for Table 5 (intra-day) but for site TOR

722 **References**

- 723 Aicardi, D., Musé, P., Alonso-Suárez, R., 2022. A comparison of satellite cloud motion vectors techniques
724 to forecast intra-day hourly solar global horizontal irradiation. *Solar Energy* 233, 46–60.
- 725 Alessandrini, S., Delle Monache, L., Sperati, S., Cervone, G., 2015. An analog ensemble for short-term
726 probabilistic solar power forecast. *Applied Energy* 157, 95–110.
- 727 Alonso-Suárez, R., Aicardi, D., Marchesoni-Acland, F., 2022. Analysis of persistence-based solar irradiance
728 forecasting benchmarks. 2203.13819.
- 729 Alonso-Suárez, R., David, M., Branco, V., Lauret, P., 2020. Intra-day solar probabilistic forecasts including
730 local short-term variability and satellite information. *Renewable Energy* 158, 554–573.
- 731 Antonanzas, J., Osorio, N., Escobar, R., Urraca, R., Martinez-de Pison, F., Antonanzas-Torres, F., 2016.
732 Review of photovoltaic power forecasting. *Solar Energy* 136, 78–111.
- 733 Bacher, P., Madsen, H., Nielsen, H.A., 2009. Online short-term solar power forecasting. *Solar Energy* 83,
734 1772–1783.
- 735 Ben Bouallègue, Z., 2015. Assessment and added value estimation of an ensemble approach with a focus on
736 global radiation forecasts. *MAUSAN* , 541–550.
- 737 Blaga, R., Sabadus, A., Stefu, N., Dughir, C., Paulescu, M., Badescu, V., 2019. A current perspective on the
738 accuracy of incoming solar energy forecasting. *Progress in Energy and Combustion Science* 70, 119–144.

739 Bollerslev, T., 1986. Generalized autoregressive conditional heteroskedasticity. *Journal of Econometrics* 31,
740 307–327.

741 Bourges, B. (Ed.), 1992. *Climatic Data Handbook for Europe*. 13537, Europäische Kommission, Dordrecht:
742 Kluwer Acad. Publ. Available online at <http://bookshop.europa.eu/en/-pbEUNA13537/>.

743 Bröcker, J., Smith, L.A., 2007. Increasing the Reliability of Reliability Diagrams. *Weather and Forecasting*
744 22, 651–661.

745 BSRN, 2024. World radiation monitoring center (wrmc), the central archive of the baseline surface radiation
746 network (bsrn). <https://bsrn.awi.de>. Accessed: 22 January 2024.

747 Carrière, T., Amaro E Silva, R., Zhuang, F., Saint-Drenan, Y.M., Blanc, P., 2021. A New Approach for
748 Satellite-Based Probabilistic Solar Forecasting with Cloud Motion Vectors. *Energies* 14, 4951.

749 Chow, C.W., Belongie, S., Kleissl, J., 2015. Cloud motion and stability estimation for intra-hour solar
750 forecasting. *Solar Energy* 115, 645–655.

751 CIEMAT, 2024. Ciemat plataforma solar de almería - europe’s biggest test center for concentrating solar
752 power (csp). <https://www.dlr.de/sf/en/desktopdefault.aspx/>. Accessed: 22 January 2024.

753 David, M., Mazorra Aguiar, L., Lauret, P., 2018. Comparison of intraday probabilistic forecasting of solar
754 irradiance using only endogenous data. *International Journal of Forecasting* 34, 529–547.

755 David, M., Ramahatana, F., Trombe, P., Lauret, P., 2016. Probabilistic forecasting of the solar irradiance
756 with recursive ARMA and GARCH models. *Solar Energy* 133, 55–72.

757 Delle Monache, L., Eckel, F., Rife, D., Nagarajan, B., Searight, K., 2013. Probabilistic weather prediction
758 with an analog ensemble. *Monthly Weather Review* 141, 3498–3516.

759 Doubleday, K., Van Scyoc Hernandez, V., Hodge, B., 2020. Benchmark probabilistic solar forecasts: Char-
760 acteristics and recommendations. *Solar Energy* 206, 52–67.

761 Dumortier, D., 1995. Modelling global and diffuse horizontal irradiances under cloudless skies with different
762 turbidities. Final Report Vol. 2. Daylight II, JOU2-CT92-0144.

763 Engle, R.F., 1982. Autoregressive conditional heteroscedasticity with estimates of the variance of united
764 kingdom inflation. *Econometrica* 50, 987–1007. Publisher: [Wiley, Econometric Society].

765 Forstinger, A., Wilbert, S., Jensen, A., Kraas, B., Peruchena, C., Gueymard, C., Ronzio, D., Yang, D.,
766 Collino, E., Martinez, J., Ruiz-Arias, J., Hanrieder, N., Blanc, P., Saint-Drenan, Y., 2021. Expert quality
767 control of solar radiation ground data sets, in: *Proceedings of SWC 2021: ISES Solar World Congress,*
768 *International Solar Energy Society*. pp. 1037–1048. SWC 2021: ISES Solar World Congress ; Conference
769 date: 25-10-2021 Through 29-10-2021.

770 Gneiting, T., Lerch, S., Schulz, B., 2023. Probabilistic solar forecasting: Benchmarks, post-processing,
771 verification. *Solar Energy* 252, 72–80.

772 Gneiting, T., Raftery, A.E., 2007. Strictly Proper Scoring Rules, Prediction, and Estimation. *Journal of the*
773 *American Statistical Association* 102, 359–378.

774 Grantham, A., Gel, Y.R., Boland, J., 2016. Nonparametric short-term probabilistic forecasting for solar
775 radiation. *Solar Energy* 133, 465–475.

776 Hammer, A., Heinemann, D., Hoyer-Klick, C., Kuhlemann, R., Lorenz, E., Müller, R., Beyer, H.G., 2003.
777 Solar energy assessment using remote sensing technologies. *Remote Sensing of Environment* 86, 423–432.

778 Hersbach, H., 2000. Decomposition of the Continuous Ranked Probability Score for Ensemble Prediction
779 Systems. *Weather and Forecasting* 15, 559–570.

780 Hong, T., Pinson, P., Fan, S., Zareipour, H., Troccoli, A., Hyndman, R.J., 2016. Probabilistic energy fore-
781 casting: Global Energy Forecasting Competition 2014 and beyond. *International Journal of Forecasting*
782 32, 896–913.

783 Hong, T., Pinson, P., Wang, Y., Weron, R., Yang, D., Zareipour, H., 2020. Energy forecasting: A review
784 and outlook. *IEEE Open Access Journal of Power and Energy* 7, 376–388.

785 IEA-PVPS-T16, 2024. Solar resource for high penetration and large scale applica-
786 tions. [https://iea-pvps.org/research-tasks/solar-resource-for-high-penetration-
787 and-large-scale-applications/](https://iea-pvps.org/research-tasks/solar-resource-for-high-penetration-and-large-scale-applications/). Accessed: 22 January 2024.

788 IEA-SHC-T46, 2024. Solar resource assessment and forecasting. <https://task46.iea-shc.org>. Accessed:
789 22 January 2024.

- 790 Iversen, E.B., Morales, J.M., Møller, J.K., Madsen, H., 2015. Short-term probabilistic forecasting of wind
791 speed using stochastic differential equations. *International Journal of Forecasting* .
- 792 Jensen, A.R., Anderson, K.S., Holmgren, W.F., Mikofski, M.A., Hansen, C.W., Boeman, L.J., Loonen, R.,
793 2023. pvlib iotools,- open-source python functions for seamless access to solar irradiance data. *Solar*
794 *Energy* 266, 112092.
- 795 Jung, J., Broadwater, R.P., 2014. Current status and future advances for wind speed and power forecasting.
796 *Renewable and Sustainable Energy Reviews* 31, 762–777.
- 797 Junk, C., Delle Monache, L., Alessandrini, S., Cervone, G., Bremen, L., 2015. Predictor-weighting strategies
798 for probabilistic wind power forecasting with an analog ensemble. *Meteorologische Zeitschrift* 24, 361–379.
- 799 Koenker, R., 2005. Quantile Regression. volume 38 of *Econometric Society Monographs*. Cambridge Uni-
800 versity Press, Cambridge.
- 801 Koenker, R., Bassett, G., 1978. Regression Quantiles. *Econometrica* 46, 33–50.
- 802 Kühnert, J., Lorenz, E., Heinemann, D., 2013. Satellite-based irradiance and power forecasting for the
803 german energy market. *Solar Energy Forecasting and Resource Assessment* , 267–295.
- 804 Lauret, P., Alonso-Suárez, R., Le Gal La Salle, J., David, M., 2022. Solar forecasts based on the clear sky
805 index or the clearness index: Which is better? *Solar* 2, 432–444.
- 806 Lauret, P., David, M., Pedro, H., 2017. Probabilistic Solar Forecasting Using Quantile Regression Models.
807 *Energies* 10, 1591.
- 808 Lauret, P., David, M., Pinson, P., 2019. Verification of solar irradiance probabilistic forecasts. *Solar Energy*
809 194, 254–271.
- 810 Lauret, P., Voyant, C., Soubdhan, T., David, M., Poggi, P., 2015. A benchmarking of machine learning
811 techniques for solar radiation forecasting in an insular context. *Solar Energy* 112, 446–457.
- 812 Le Gal La Salle, J., David, M., Lauret, P., 2021. A new climatology reference model to benchmark proba-
813 bilistic solar forecasts. *Solar Energy* 223, 398–414.
- 814 Lefèvre, M., Oumbe, A., Blanc, P., Espinar, B., Gschwind, B., Qu, Z., Wald, L., Schroedter-Homscheidt,
815 M., Hoyer-Klick, C., Arola, A., Benedetti, A., Kaiser, J.W., Morcrette, J.J., 2013. McClear: a new model
816 estimating downwelling solar radiation at ground level in clear-sky conditions. *Atmospheric Measurement*
817 *Techniques* 6, 2403–2418.
- 818 Liu, C., 2009. Beyond Pixels: Exploring New Representations and Applications for Motion Analysis. Ph.D.
819 thesis. Massachusetts Institute of Technology. Cambridge, MA, USA.
- 820 Lorenz, E., Remund, J., Müller, S.C., Traunmüller, W., Steinmaurer, G., Pozo, D., Ruiz-Arias, J.A., Fanego,
821 V.L., Ramirez, L., Romeo, M.G., Kurz, C., Pomares, L.M., Geijo Guerrero, C., 2009. Benchmarking of
822 different approaches to forecast solar irradiance, in: 24th European photovoltaic solar energy conference,
823 Hamburg Germany. pp. 21–25.
- 824 Lorenz, E., Ruiz-Arias, J.A., Martin, L., Wilbert, S., Köhler, C., Fritz, R., Betti, A., Lauret, P., David, M.,
825 Huang, J., Perez, R., Kazantzidis, A., Wang, P., Saint-Drenan, Y.M., 2021. Forecasting Solar Radiation
826 and Photovoltaic Power. NREL/TP-5D00-77635, National Renewable Energy Laboratory, Golden, CO.
- 827 Mazorra-Aguiar, L., Lauret, P., David, M., Oliver, A., Montero, G., 2021. Comparison of Two Solar
828 Probabilistic Forecasting Methodologies for Microgrids Energy Efficiency. *Energies* 14, 1679.
- 829 Meinshausen, N., Ridgeway, G., 2006. Quantile regression forests. *Journal of Machine Learning Research* 7,
830 983–999.
- 831 Morales, J.M., Conejo, A.J., Madsen, H., Pinson, P., Zugno, M., 2014. Integrating Renewables in Electricity
832 Markets. volume 205 of *International Series in Operations Research & Management Science*. Springer
833 US, Boston, MA. DOI: 10.1007/978-1-4614-9411-9.
- 834 Notton, G., Nivet, M.L., Voyant, C., Paoli, C., Darras, C., Motte, F., Fouilloy, A., 2018. Intermittent
835 and stochastic character of renewable energy sources: Consequences, cost of intermittence and benefit of
836 forecasting. *Renewable and Sustainable Energy Reviews* 87, 96–105.
- 837 Paletta, Q., Arbod, G., Lasenby, J., 2021. Benchmarking of deep learning irradiance forecasting models
838 from sky images ,À an in-depth analysis. *Solar Energy* 224, 855–867.
- 839 Paletta, Q., Arbod, G., Lasenby, J., 2023. Omnivision forecasting: Combining satellite and sky images for
840 improved deterministic and probabilistic intra-hour solar energy predictions. *Applied Energy* 336, 120818.

- 841 Pedro, H.T., Coimbra, C.F., 2012. Assessment of forecasting techniques for solar power production with no
842 exogenous inputs. *Solar Energy* 86, 2017–2028.
- 843 Pedro, H.T.C., Larson, D.P., Coimbra, C.F.M., 2019. A comprehensive dataset for the accelerated develop-
844 ment and benchmarking of solar forecasting methods. *Journal of Renewable and Sustainable Energy* 11,
845 036102.
- 846 Pinson, P., McSharry, P., Madsen, H., 2010. Reliability diagrams for non-parametric density forecasts of
847 continuous variables: Accounting for serial correlation. *Quarterly Journal of the Royal Meteorological*
848 *Society* 136, 77–90.
- 849 Pinson, P., Nielsen, H.A., Møller, J.K., Madsen, H., Kariniotakis, G.N., 2007. Non-parametric probabilistic
850 forecasts of wind power: required properties and evaluation. *Wind Energy* 10, 497–516.
- 851 Qu, Z., Oumbe, A., Blanc, P., Espinar, B., Gesell, G., Gschwind, B., Klüser, L., Lefèvre, M., Saboret, L.,
852 Schroedter-Homscheidt, M., Wald, L., 2017a. Fast radiative transfer parameterisation for assessing the
853 surface solar irradiance: The heliosat?4 method. *Meteorologische Zeitschrift* 26, 33–57.
- 854 Qu, Z., Oumbe, A., Blanc, P., Espinar, B., Gesell, G., Gschwind, B., Klüser, L., Lefèvre, M., Saboret, L.,
855 Schroedter-Homscheidt, M., Wald, L., 2017b. Fast radiative transfer parameterisation for assessing the
856 surface solar irradiance: The heliosat?4 method. *Meteorologische Zeitschrift* 26, 33–57.
- 857 Raschka, S., Mirjalili, V., 2019. *Python Machine Learning: Machine Learning and Deep Learning with*
858 *Python, scikit-learn, and TensorFlow 2*. Packt Publishing Ltd, Birmingham. third edition.
- 859 Sobri, S., Koochi-Kamali, S., Rahim, N.A., 2018. Solar photovoltaic generation forecasting methods: A
860 review. *Energy Conversion and Management* 156, 459–497.
- 861 Taylor, J.W., 2004. Volatility forecasting with smooth transition exponential smoothing. *International*
862 *Journal of Forecasting* 20, 273–286.
- 863 Tsay, R.S., 2010. *Analysis of Financial Time Series*. Wiley Series in Probability and Statistics, Wiley. 1
864 edition.
- 865 van der Meer, D., Widén, J., Munkhammar, J., 2018. Review on probabilistic forecasting of photovoltaic
866 power production and electricity consumption. *Renewable and Sustainable Energy Reviews* 81, 1484–
867 1512.
- 868 Verbois, H., Saint-Drenan, Y.M., Thiery, A., Blanc, P., 2022. Statistical learning for nwp post-processing:
869 A benchmark for solar irradiance forecasting. *Solar Energy* 238, 132–149.
- 870 Visser, L., AlSkaif, T., Hu, J., Louwen, A., van Sark, W., 2023. On the value of expert knowledge in
871 estimation and forecasting of solar photovoltaic power generation. *Solar Energy* 251, 86–105.
- 872 Wilks, D.S., 2009. *Statistical methods in the atmospheric sciences*. Number 91 in *International geophysics*
873 *series*, Elsevier [u.a.], Amsterdam. 2. ed., [nachdr.] edition. OCLC: 845720508.
- 874 Yang, D., van der Meer, D., Munkhammar, J., 2020. Probabilistic solar forecasting benchmarks on a
875 standardized dataset at folsom, california. *Solar Energy* 206, 628–639.
- 876 Yang, D., Wang, W., Gueymard, C.A., Hong, T., Kleissl, J., Huang, J., Perez, M.J., Perez, R., Bright,
877 J.M., Xia, X., van der Meer, D., Peters, I.M., 2022. A review of solar forecasting, its dependence on
878 atmospheric sciences and implications for grid integration: Towards carbon neutrality. *Renewable and*
879 *Sustainable Energy Reviews* 161, 112348.